

Real-Time PID Control Strategy for Maglev Transportation System via Particle Swarm Optimization

Rong-Jong Wai, *Senior Member, IEEE*, Jeng-Dao Lee, *Member, IEEE*, and Kun-Lun Chuang

Abstract—This paper focuses on the design of a real-time particle-swarm-optimization-based proportional-integral-differential (PSO-PID) control scheme for the levitated balancing and propulsive positioning of a magnetic-levitation (maglev) transportation system. The dynamic model of a maglev transportation system, including levitated electromagnets and a propulsive linear induction motor based on the concepts of mechanical geometry and motion dynamics, is first constructed. The control objective is to design a real-time PID control methodology via PSO gain selections and to directly ensure the stability of the controlled system without the requirement of strict constraints, detailed system information, and auxiliary compensated controllers despite the existence of uncertainties. The effectiveness of the proposed PSO-PID control scheme for the maglev transportation system is verified by numerical simulations and experimental results, and its superiority is indicated in comparison with PSO-PID in previous literature and conventional sliding-mode (SM) control strategies. With the proposed PSO-PID control scheme, the controlled maglev transportation system possesses the advantages of favorable control performance without chattering phenomena in SM control and robustness to uncertainties superior to fixed-gain PSO-PID control.

Index Terms—Linear induction motor (LIM), maglev transportation system, magnetic levitation (maglev), particle swarm optimization (PSO), proportional integral differential (PID), sliding-mode (SM) control.

I. INTRODUCTION

IN RECENT years, many magnetic-levitation (maglev) transportation systems have been constructed, tested, and improved [1]. In general, a maglev transportation system can be divided into propulsion and levitation mechanisms. Linear induction motors (LIMs) have many excellent performance features such as a high-starting thrust force, alleviation of the gear between the motor and the motion devices, reduction of the mechanical losses and the size of motion devices, high-

speed operation, and silence [2]. Owing to these advantages, the LIM has been used widely in the field of industrial processes and transportation applications [3]. Because the LIM can be visualized to unroll a rotary induction motor (RIM), the driving principles of the LIM are similar to the RIM, and the dynamic model of the LIM could be modified from the one of the RIM. Thus, many decoupled control techniques in RIM, such as field-orientated control [4] and nonlinear state feedback techniques [5], can be adopted to decouple the dynamics of the thrust and the flux amplitude of the LIM. In this paper, the LIM is used as the propulsive mechanism, and a simple decoupled dynamic of the LIM, with the possible occurrence of uncertainties, is considered in the entire dynamic model of the maglev transportation system.

Nowadays, maglev techniques have been manipulated in eliminating friction due to mechanical contact, in decreasing the maintaining cost, and in achieving high-precision positioning. Therefore, they have been widely used in the maglev transportation systems [6]–[9]. In general, the maglev techniques can be classified into two categories, namely, electrodynamic suspension (EDS) and electromagnetic suspension (EMS). EDS systems are commonly known as “repulsive levitation,” and the corresponding levitation sources are from superconductivity [8] or permanent magnets [9]. However, the repulsive magnetic poles of superconductivity magnets cannot be activated at low speed so that they are only suitable for long-distance and high-speed train systems. Basically, the maglev force of EDS is partially stable, and it allows a large clearance. Nevertheless, the production process of magnetic materials is more complex and expensive. On the other hand, EMS systems are commonly known as “attractive levitation,” and the maglev force is inherently unstable so that the control problem becomes more difficult. In this paper, the EMS strategy is utilized for the fundamental levitation force of a maglev transportation system, and the corresponding levitated positioning and stabilizing control of the maglev system is one of the major control objectives to be manipulated.

Because the EMS system has unstable and nonlinear behaviors, it is difficult to build a precise dynamic model. Some research has derived various mathematical models for many kinds of maglev systems [10], [11], but there still exists unmodeled dynamics or unpredictable uncertainties in practical applications. In general, linearized control strategies based on a Taylor-series expansion of the actual nonlinear dynamic model and force distribution at nominal operating points are often employed. Nevertheless, the tracking performances of

Manuscript received November 4, 2009; revised January 15, 2010; accepted March 7, 2010. Date of publication March 22, 2010; date of current version January 12, 2011. This work was supported in part by the National Science Council of Taiwan under Grant NSC 97-2221-E-155-065-MY2.

R.-J. Wai is with the Department of Electrical Engineering and Fuel Cell Center, Yuan Ze University, Chung Li 32003, Taiwan (e-mail: rjwai@saturn.yzu.edu.tw; s954608@mail.yzu.edu.tw).

J.-D. Lee is with the Department of Automation Engineering, National Formosa University, Yunlin 632, Taiwan (e-mail: jengdaolee@hotmail.com).

K.-L. Chuang was with the Department of Electrical Engineering and Fuel Cell Center, Yuan Ze University, Chung Li 32003, Taiwan. He is now with the Ministry of National Defense, Taipei, Taiwan. (e-mail: s954608@mail.yzu.edu.tw).

Color versions of one or more of the figures in this paper are available online at <http://ieeexplore.ieee.org>.

Digital Object Identifier 10.1109/TIE.2010.2046004

linearized control strategies [12], [13] deteriorate rapidly with an increasing deviation from nominal operating points. Many approaches that are introduced to solve this problem for ensuring consistent performances that are independent of the operating points have been reported in previous literature. Recursive backstepping methods were reported in [7] and [14] due to the systematic design procedure. Kaloust *et al.* [7] proposed a recursive control in the sense of nonlinear state transformation and Lyapunov's direct method to guarantee global stability for a nonlinear maglev system. However, this nonlinear robust control for the levitation and propulsion of a maglev system was individually designed. Queiroz and Dawson [14] utilized a nonlinear model of an active magnetic bearing system in developing a nonlinear backstepping controller. Unfortunately, partial constrained conditions should be satisfied for precise positioning. On the other hand, the attractive levitation in the EMS system belongs to a nonnegative input system. Some researches focused on nonnegative input systems that are addressed in [15]. Overall, partial mathematical models via complicated modeling processes or specific mechatronic device are usually required to design a suitable control law for achieving positioning demand. Recently, Wai and Lee [16] have proposed three model-free control strategies including a simple proportional-integral-differential (PID) control, a fuzzy-neural-network (FNN) control, and an adaptive control for the positioning of a hybrid magnetic maglev system. In [16], control gains in the PID control scheme are not easy to be decided, and the FNN control framework is more complex. Although the adaptive control in [16] possesses online learning ability and simple control framework, the adaptation laws in this control system are always positive, and the electromagnets will eventually be saturated. In addition, Wai and Lee [17] presented adaptive sliding-mode (SM) control and adaptive FNN control schemes for the levitation and propulsion control of a maglev transportation system. However, no related experimental results were reported in [17]. The real-time implementation may be difficult or impossible due to a heavy computation burden if the network parameters to be tuned or inference strategies are complicated. After reviewing the typical approaches for the maglev transportation system [6]–[17], some conclusions about the design methods of the control systems for the maglev can be obtained. First, the controller design in previous literatures [7]–[14] are always dependent on certain system information. Moreover, the specific and complex structure in [15] was constructed to solve a nonnegative input problem about the positioning issue via electromagnets. For releasing the requirement of the system information, there are many efficient control strategies (e.g., [16], [17]) that are developed to deal with this difficult control problem recently. However, these control methods still have the problem of electromagnetic saturation or heavy computation burden such that they are hard to be adopted in practical applications. To compare typical approaches [6]–[17] with the control framework that is to be developed in this paper, the proposed control scheme not only has the learning ability that is similar to intelligent control, but also, its control framework that is similar to the traditional PID controller is simpler than the intelligent control. Moreover, the normal operation for electromagnets and the decreasing

computation burden will be helpful in accomplishing a real-time maglev transportation control system.

In the initial stages, particle swarm optimization (PSO) is not a very efficient method when it is applied to solving the real-world problems; its being time consuming is the key issue in the applications. Owing to gradually developed research, PSO has recently received much interest in achieving high efficiency and in searching global optimal solution in problem spaces [18]–[26]. The PSO is an evolutionary computation technique developed by Eberhart and Kennedy in 1995 [18], [19], inspired by social behavior of bird flocking. Similar to the genetic algorithm (GA) [27], the PSO algorithm is an optimization tool based on population, and the system is initialized with a population of random solution. It can search for optima by the updating of generations. Unlike the GA, the PSO algorithm has no complicated evolutionary operators such as crossover and mutation. In the PSO algorithm, the potential solution acts as a particle, and it simulates how natural creatures behave as a swarm. Every particle has a fitness value, which is evaluated by the fitness function to be optimized, and a velocity that directs the trajectory of the particle. By this way, the individual particles are ultimately attracted toward their previous best location and the swarm's best solution in searching space. In 1998, Shi and Eberhart [20] introduced varied inertial weights during different searching stages into the previous PSO algorithm to bring in a significant improvement on the PSO performance. Although the inertia weights in [20] were adjusted by using deterministic rules according to the generations, the feedback information from the search process was not used [21]. Zhan *et al.* [22] proposed an adaptive PSO algorithm to adjust the parameters in a control procedure according to the feedback information of the search process, and it was proven that a better search efficiency than classical PSO can be obtained. Ling *et al.* [23] presented hybrid PSO-based wavelet neural network for modeling the development of fluid dispensing for electronic packaging. A method of nonlinear identification based on the Takagi–Sugeno (TS) fuzzy model and optimization procedure was investigated in [24], and chaotic PSO algorithms were used for the design of the premise part of production rules, while the least-mean-square technique was utilized for the subsequent part of production rules of the TS fuzzy model. Feng [25] developed a powerful evolutionary PSO learning algorithm to automatically generate the parameters for a radial basis function neural network. Chatterjee *et al.* [26] proposed the possible development of PSO-based FNNs that can be employed as an important building block in real robot systems, controlled by voice-based commands. However, the role of PSO is usually used as a minor compensatory tuner in the previous literatures [18]–[26] because the stability of a PSO-based control scheme cannot be guaranteed. Gaing [28] presented a novel design method for determining the optimal PID controller parameters by using the PSO algorithm. Lin *et al.* [29] designed a recurrent functional-link-based FNN controller with improved PSO to control a three-phase induction-generator system for stand-alone power application. Although the system stability in [28] and [29] can be guaranteed, the role of PSO is still used as a minor role. In order to overcome the aforementioned problems, the motivation of this paper is to develop a real-time PSO control

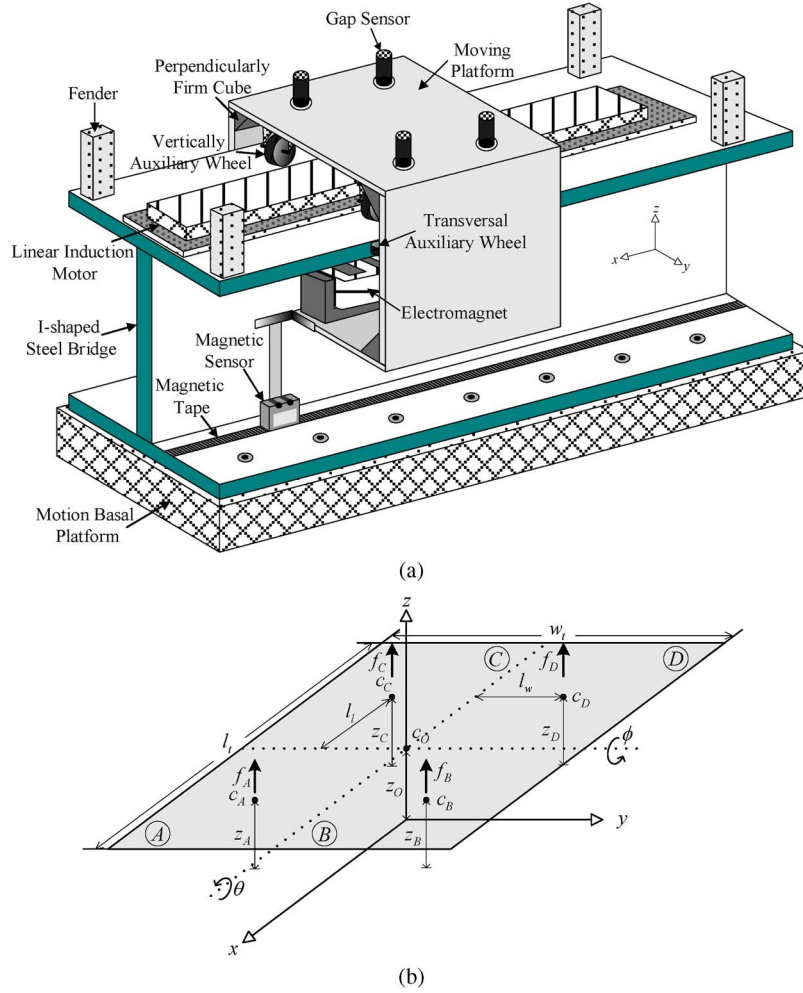


Fig. 1. (a) Entire framework of the maglev transportation system. (b) Sketch diagram of the maglev system.

scheme to directly ensure the stability of the controlled system without the requirement of strict constraints, detailed system information, and auxiliary compensated controllers despite the existence of uncertainties.

SM control is one of the effective nonlinear robust control approaches since it provides fast system dynamic responses with an invariance property to uncertainties once the system dynamics are controlled in the SM [30]–[32]. Gutierrez and Ro [33] presented an SM control design for a magnetic servo levitation system to possess the robustness with respect to parametric uncertainties and unmodeled dynamics. Bandyopadhyay *et al.* [34] designed an SM observer based on high gain to reconstruct the states of the system for the implementation of SM control. Unfortunately, the information of system uncertainties is usually required in conventional SM control strategies. In previous research literature [35], [36], various adaptive estimation mechanisms for uncertainty information have been embedded in SM control to be capable of keeping the robustness proposed with respect to system uncertainties. Li *et al.* [35] proposed an adaptive SM flux observer for the sensorless speed control of induction motors. Wai and Chang [36] implemented an adaptive SM control system to control a dual-axis inverted-pendulum mechanism that is driven by permanent magnet synchronous motors. Although these control strategies had good

control performances and were insensitive to uncertainties, adaptive estimation algorithms for system uncertainties are always monotonous functions, and tracking errors introduced by any uncertainty, such as sensor error or accumulation of numerical error, will cause the estimated values to increase even to infinity with time. As a result, actuators will eventually be saturated, and the controlled system may be unstable.

In general, conventional PID-type controllers have been widely used in industry due to their simple control structure, easy design, and inexpensive cost. However, the PID-type controller cannot provide a perfect control performance if the controlled plant is highly nonlinear and uncertain. In other words, the PID parameters usually need manual retuning before being transferred to the process under control. The innovative idea of this paper is to design a real-time control scheme that possesses the evolutionary capability of the PSO, the robust ability of the SM control, and the simple control structure similar to the conventional PID controller.

II. DYNAMIC ANALYSES OF MAGLEV TRANSPORTATION SYSTEM

The entire framework of a maglev transportation system is shown in Fig. 1(a), which is a linear motor via EMS

technique that is used to reduce friction forces during linear movement for promoting electric machinery efficiency and simplifying the mechanical design procedure [17]. The bottom of this mechanism is a motion basal platform equipped with an I-shaped steel bridge as the rail body. The motion basal platform is a granite foundation that keeps the mechanism horizontal. By appropriately exciting the stator winding of a LIM that is fixed on the overhead I-shaped steel bridge, it will produce the thrust force to propel the moving platform in a horizontal displacement, and the corresponding displacement can be measured by a magnetic sensor moved along a magnetic tape. Moreover, the fenders that are placed at the ends of the LIM are designed to avoid the problem of collision, and vertically auxiliary wheels are used to decrease friction forces before the moving platform has been suspended completely. In order to achieve the maglev object, four electromagnets under the bottom of the moving platform are adopted in this paper. When the electromagnets are excited to attract the upper plate of the rail, the moving platform will be levitated, and the corresponding levitation height is acquired by a gap sensor. In addition, perpendicularly firm cubes are installed for holding the vertical angle between two conductor plates of the moving platform to reduce measure errors. When the transversal displacement is varied during linear movement, transversal auxiliary wheels are employed to guide the moving platform on the march.

In general, six degrees-of-freedom (DOF) could be considered in a fully suspended substance. For decreasing the hardware cost, the transversal electromagnets and gap sensors are replaced by transversal auxiliary wheels in this paper. According to Fig. 1(a), rotating along the z -axis and moving in the y -direction are constricted by transversal auxiliary wheels, which will result in little friction forces during the moving process. Therefore, three kinds of motions including levitation (z_O , moving in the z -direction), rolling (θ , rotating along the x -axis), and pitching (ϕ , rotating along the y -axis) are at least needed to be considered to analyze the dynamic model of the maglev system. In other words, the mechanical behavior is constrained on the side-to-side movements, and it only takes into account the reliance on the levitation, roll, and pitch in the dynamic derivation. To regard the moving platform as a 3-D coordinate of the levitation stage, the sketch diagram of the maglev system is shown in Fig. 1(b), where l_t and w_t are the length and width of the moving platform. c_O , which is located at the z -axis ($x = 0, y = 0$) in the 3-D coordinate, denotes the mass center of the moving platform. z_O and $z_{O,\max}$ are the central levitation height and its maximum limitation. By dividing the moving platform equally into four subplatforms labeled as A, B, C , and D areas, c_A, c_B, c_C , and c_D represent the mass centers of four subplatforms, and the corresponding levitation heights labeled as z_A, z_B, z_C , and z_D are measured via the gap sensors that are installed in the location of the individual mass center. l_w and l_l are the horizontal distances from the mass centers of the four subplatforms to the x - and y -axes, respectively. The applied control force vector is represented as $\mathbf{f} = [f_A \ f_B \ f_C \ f_D \ F_{\lim}]^T$, in which f_A, f_B, f_C , and f_D of the four subplatforms are acquired through levitation forces produced by electromagnets, and F_{\lim} is the

propulsive force produced by the LIM. In general, a maglev force can be expressed as [16]

$$f_e(x_e, i_e) = -\frac{1}{2} \left(\frac{\partial P}{\partial x_e} \right) N_m^2 i_e^2 \equiv G_f i_e^2 \quad (1)$$

where x_e and P are the air-gap length and permeance of the electromagnet; N_m and i_e are the turn number and magnetizing current of the electromagnetic coil. In (1), the partial differential term $\partial P / \partial x_e$ can be extended as

$$\frac{\partial P}{\partial x_e} = \frac{-2 (\partial R_{x_e} / \partial x_e)}{(R_{x_e} + R_{Fe} + R_c)^2} \quad (2)$$

where R_{x_e}, R_{Fe} , and R_c are the reluctances of the ferrous plate, core, and air-gap length, respectively. Moreover, the reluctances in (2) can be represented as

$$R_{x_e} = h_x x_e \quad R_{Fe} = h_{Fe} \quad R_c = h_c \quad (3)$$

where h_x is a function of the permeability of the air gap and the cross-sectional areas passed by the flux in the air gap, h_{Fe} is dependent on the permeability of the ferrous plate and the cross-sectional areas and the length passed by the flux in the ferrous plate, and h_c is related to the permeability of the core and the cross-sectional areas and the length passed by the flux in the ferrous plate and the core. Note that the values of h_x, h_{Fe} , and h_c in (3) are positive. According to (2) and (3), the maglev force in (1) can be reformulated as

$$\begin{aligned} f_e(x_e, i_e) &= -\frac{1}{2} \frac{-2 (\partial R_{x_e} / \partial x_e)}{(R_x + R_{Fe} + R_c)^2} N_m^2 i_e^2 \\ &= \left(\frac{1}{h_2 x_e^2 + h_1 x_e + h_0} \right) i_e^2 \equiv G_f i_e^2 \quad (4) \end{aligned}$$

where $h_2 = h_x / N_m^2 > 0$, $h_1 = 2(h_{Fe} + h_c) / N_m^2 > 0$, and $h_0 = (h_{Fe} + h_c)^2 / (h_x N_m^2) > 0$. In addition, a nonlinear characteristic of the force will be performed by the electromagnet, with the variable air-gap length in motion. Moreover, the gain (G_f) of the maglev force is influenced not only by the air-gap length but also by the variation of the permeability in different operating points. Note that permeability is not easy to obtain precisely; therefore, the variation of the electromagnet gain due to the permeability that is changed with different operation points will be considered into the lumped uncertainty in this paper. In practice, there will exist some uncertainties in the maglev force, such as changing temperature within the coil, which will inevitably result in modeling errors (G_f is not a constant). Therefore, the controller that is to be developed should be robust enough to tolerate these uncertainties and unmodeled dynamics. According to (1), the levitation forces produced by four electromagnets in this maglev system can be represented as follows:

$$\begin{aligned} f_A(x_{e_A}, i_A) &= -\frac{1}{2} \frac{\partial P_A}{\partial x_{e_A}} N_{m_A}^2 i_A^2 \equiv G_A i_A^2, \\ f_B(x_{e_B}, i_B) &= -\frac{1}{2} \frac{\partial P_B}{\partial x_{e_B}} N_{m_B}^2 i_B^2 \equiv G_B i_B^2, \\ f_C(x_{e_C}, i_C) &= -\frac{1}{2} \frac{\partial P_C}{\partial x_{e_C}} N_{m_C}^2 i_C^2 \equiv G_C i_C^2, \\ f_D(x_{e_D}, i_D) &= -\frac{1}{2} \frac{\partial P_D}{\partial x_{e_D}} N_{m_D}^2 i_D^2 \equiv G_D i_D^2 \quad (5) \end{aligned}$$

where the symbols with suffixes A, B, C , and D indicate the variables for the four electromagnets in different areas.

According to the Lagrangian method, the dynamic model of the maglev system is derived in Appendix A. By considering the mechanical equation of the propulsive LIM in Appendix B, the entire dynamic model of a maglev transportation system can be organized by the following matrix form [17]:

$$\mathbf{M}_0 \ddot{\mathbf{x}} + \mathbf{B}_0 \dot{\mathbf{x}} = \mathbf{u}_c - \mathbf{d}_0 \quad (6)$$

where \mathbf{M}_0 denotes the mass and inertia matrix including the total mass and the inertia with respect to the x - and y -axes of the moving platform, \mathbf{B}_0 expresses the viscosity matrix in relation to the viscosity and iron-loss coefficient of the LIM, and \mathbf{d}_0 is the gravity vector, which is influenced by the total mass of the moving platform. The detailed elements of matrices \mathbf{M}_0 and \mathbf{B}_0 , and vector \mathbf{d}_0 are given in Appendix C. The system position vector $\mathbf{x} = [z_O \ \theta \ \phi \ \kappa \ x_m]^T$ and its derivative ($\dot{\mathbf{x}}$) are assumed to be available. $\mathbf{u}_c = [u_{F_z} \ u_{T_\theta} \ u_{T_\phi} \ u_{T_\kappa} \ u_{F_{lim}}]^T$ is the attitude control force vector acquired by the levitation forces produced by electromagnets and the propulsive force produced by the LIM. Note that the bending angle κ is regarded as a zero state in this paper because the moving platform is assumed to be a rigid body. The relation between the attitude control force and the actual control current can be represented as

$$\mathbf{u}_c = \mathbf{G}_g \mathbf{G}_s \mathbf{u} \quad (7)$$

where $\mathbf{u} = [i_A^2 \ i_B^2 \ i_C^2 \ i_D^2 \ i_{lim}]^T$ is a control current vector, in which i_A, i_B, i_C , and i_D are the corresponding magnetizing currents for the four electromagnets and i_{lim} is the LIM

force control current; $\mathbf{G}_s = \begin{bmatrix} 1 & 1 & 1 & 1 & 0 \\ -1 & 1 & -1 & 1 & 0 \\ -1 & -1 & 1 & 1 & 0 \\ 1 & -1 & -1 & 1 & 0 \\ 0 & 0 & 0 & 0 & 1 \end{bmatrix}$; and

$\mathbf{G}_g = \Lambda_l \mathbf{G}_s \Lambda_g \mathbf{G}_s^T \Lambda_N^2$, in which $\Lambda_l = \text{diag}[1, l_w, l_l, l_d, 1]$, $\Lambda_N = \begin{bmatrix} 0.5\mathbf{I}_4 & 0 \\ 0 & 1 \end{bmatrix}$, $\Lambda_g = \text{diag}[G_A, G_B, G_C, G_D, K_f]$, with the LIM force constant K_f and the definitions of G_A, G_B, G_C , and G_D are given in (5). Moreover, the relation between the control effort and the actual control current can be represented as $\mathbf{u}_c = \mathbf{G}_g \mathbf{G}_s \mathbf{u}$ in (7). As can be seen from (5) and \mathbf{G}_g in (7), the forces will be affected by different air-gap lengths and magnetizing currents in electromagnets so that the nonlinear characteristics of the electromagnets make a challenge problem with controlling a maglev system.

After mathematical manipulations, the nominal dynamic model of the maglev transportation system with current control input can be represented as follows:

$$\mathbf{M} \ddot{\mathbf{x}} + \mathbf{B} \dot{\mathbf{x}} = \mathbf{G}_s \mathbf{u} - \mathbf{d} \quad (8)$$

where $\mathbf{B} = \mathbf{G}_g^{-1} \mathbf{B}_0$, $\mathbf{d} = \mathbf{G}_g^{-1} \mathbf{d}_0$, and $\mathbf{M} = \mathbf{G}_g^{-1} \mathbf{M}_0$. Note that the property of a positive-definite matrix \mathbf{M} will be verified in Appendix C. Since the actual measurable variables are the central levitation heights of four subplatforms, the relation

of the levitation heights (z_A, z_B, z_C, z_D) and system states (z_O, θ, ϕ) can be transferred by

$$\begin{aligned} z_A &= z_O - l_w \sin \theta - l_l \sin \phi & z_B &= z_O + l_w \sin \theta - l_l \sin \phi \\ z_C &= z_O - l_w \sin \theta + l_l \sin \phi & z_D &= z_O + l_w \sin \theta + l_l \sin \phi. \end{aligned} \quad (9)$$

By considering (8) with parameter variations and external disturbance, the actual dynamic model can be represented realistically as

$$(\mathbf{M} + \Delta \mathbf{M}) \ddot{\mathbf{x}} + (\mathbf{B} + \Delta \mathbf{B}) \dot{\mathbf{x}} = \mathbf{G}_s \mathbf{u} - (\mathbf{d} + \Delta \mathbf{d}) - \mathbf{f}_{d0} \quad (10)$$

where $\Delta \mathbf{M}$, $\Delta \mathbf{B}$, and $\Delta \mathbf{d}$ denote the uncertainties introduced by system parameters and unmodeled dynamics and \mathbf{f}_{d0} expresses the external disturbance vector in practical applications. By defining a lumped uncertainty vector as $\mathbf{l}_u = \Delta \mathbf{M} \ddot{\mathbf{x}} + \Delta \mathbf{B} \dot{\mathbf{x}} + \Delta \mathbf{d} + \mathbf{f}_{d0}$, (10) can be rewritten as

$$\mathbf{M} \ddot{\mathbf{x}} + \mathbf{B} \dot{\mathbf{x}} + \mathbf{l}_u = \mathbf{G}_s \mathbf{u} - \mathbf{d} \quad (11)$$

where the bound of the lumped uncertainty vector is assumed to be given by $\|\mathbf{l}_u\|_1 < \rho$, in which $\|\cdot\|_1$ is the 1-norm operator and ρ is a given positive constant.

III. SM CONTROL

By viewing \mathbf{u}_{SMC}^v as a virtual control effort vector (i.e., $\mathbf{u}_{SMC}^v = \mathbf{G}_s \mathbf{u} - \mathbf{d}$) and reformulating (11) as

$$\ddot{\mathbf{x}} = -\mathbf{M}^{-1} \mathbf{B} \dot{\mathbf{x}} - \mathbf{M}^{-1} \mathbf{l}_u + \mathbf{M}^{-1} \mathbf{u}_{SMC}^v. \quad (12)$$

The control problem is to find a suitable control law so that the system states can track the desired reference commands. To achieve this control objective, define an error state vector $\mathbf{e} = \mathbf{x}_d - \mathbf{x}$ and its derivative $\dot{\mathbf{e}} = \dot{\mathbf{x}}_d - \dot{\mathbf{x}}$, in which $\mathbf{x}_d = [z_{Od} \ \theta_d \ \phi_d \ \kappa_d \ x_{md}]^T$ is the reference trajectory vector specified by a reference model. In the conventional SM control design, a sliding surface vector is chosen as follows [32]:

$$\mathbf{s}_l = \dot{\mathbf{e}} + \mathbf{L} \mathbf{e} \quad (13)$$

where $\mathbf{L} = \text{diag}(\lambda_1, \lambda_2, \lambda_3, \lambda_4, \lambda_5)$, in which $\lambda_1, \lambda_2, \lambda_3, \lambda_4$, and λ_5 are all positive constants. By taking the derivative of the sliding surface vector with respect to time and by using (12), then

$$\dot{\mathbf{s}}_l = \ddot{\mathbf{x}}_d - \mathbf{M}^{-1} \mathbf{u}_{SMC}^v + \mathbf{M}^{-1} \mathbf{B} \dot{\mathbf{x}} + \mathbf{M}^{-1} \mathbf{l}_u + \mathbf{L} \dot{\mathbf{e}}. \quad (14)$$

From (14), the SM control law can be designed as

$$\mathbf{u}_{SMC}^v = \mathbf{B} \dot{\mathbf{x}} + \mathbf{M} \ddot{\mathbf{x}}_d + \mathbf{M} \mathbf{L} \dot{\mathbf{e}} + \dot{\mathbf{M}} \mathbf{s}_l / 2 + \mathbf{K}_s \mathbf{s}_l + \rho \text{sgn}(\mathbf{s}_l) \quad (15)$$

where a control gain ρ is concerned with the upper bound of uncertainties, $\text{sgn}(\cdot)$ is a sign function, and \mathbf{K}_s is a diagonal positive-definite matrix. According to the Lyapunov theorem [32], the stability of the SM control strategy can be guaranteed with $\|\mathbf{l}_u\|_1 < \rho$.

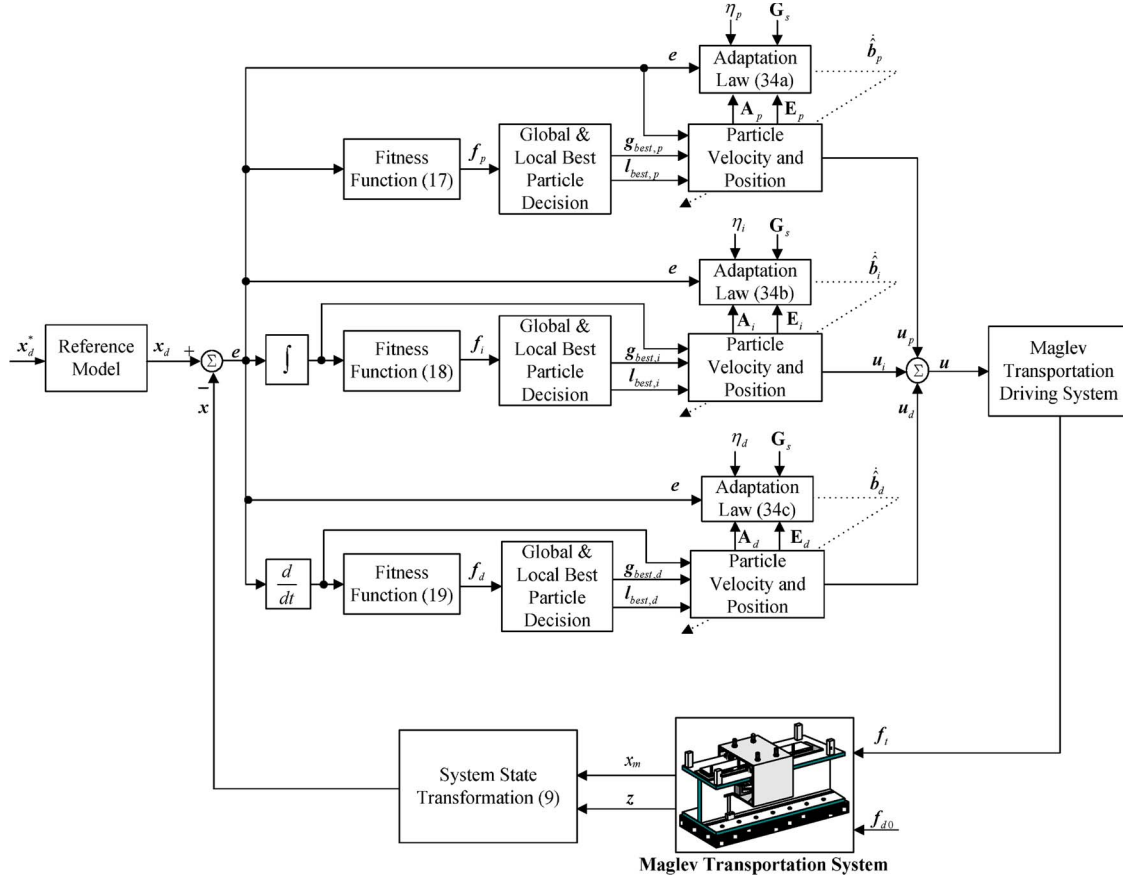


Fig. 2. PSO-PID control block diagram.

According to the relation of $\mathbf{u}_{\text{SMC}}^v = \mathbf{G}_s \mathbf{u} - \mathbf{d}$, the realistic control current vector derived from the SM control law, as shown in (15), has to be transferred by

$$\mathbf{u}_{\text{SMC}} = \mathbf{G}_s^{-1} (\mathbf{u}_{\text{SMC}}^v + \mathbf{d}). \quad (16)$$

Note that the uncertainty ($\Delta \mathbf{d}$) of the vector \mathbf{d} caused by payload variations has been considered into the lumped uncertainty vector (11). Thus, the SM control law in (16) can be realized via normal system parameters in practical applications.

The existence condition of the SM can be satisfied with $\|\mathbf{l}_u\|_1 < \rho$. A selection of the upper bound of the lumped uncertainty vector has a significant effect on the control performance. If the selection is selected to be too large, the sign function in (15) will result in serious chattering phenomena in the control efforts. The undesired chattering control efforts will wear the mechanism and might excite unstable system dynamics. On the other hand, if the selection is too small, the stability conditions may not be satisfied. It will cause the controlled system to be unstable. In addition, the control currents belong to nonnegative inputs in the EMS system. To deal with the problem of nonnegative control inputs for electromagnets, the SM control law in (15) has to be transformed to actual control currents according to (16). To ensure the stability of the controlled system despite the existence of uncertainties, to alleviate the chattering phenomena in control efforts, and to avoid redundant transformation steps, a novel PSO-based

PID (PSO-PID) control system is introduced in the following section.

IV. PSO-PID CONTROL

In this paper, the real-time PSO-PID control system, which contains PID-type control parts including a proportional control (\mathbf{u}_p), an integral control (\mathbf{u}_i), and a differential control (\mathbf{u}_d), is shown in Fig. 2. There are three kinds of real-time PSO mechanisms in the control framework, and the corresponding evolutionary methodologies are implemented according to individual fitness function vectors (\mathbf{f}_p , \mathbf{f}_i , and \mathbf{f}_d). Moreover, the PSO evolution is used to produce a suitable control effort via the imitation of the SM control, and the corresponding adaptation laws are derived in the sense of the Lyapunov theorem [32] to decide appropriate evolutionary coefficients for ensuring the stable control performance. The detailed descriptions of the major control design and the Lyapunov stability analyses are exhibited in the following sections.

A. Major Control Design

Selection of the values for the parameters in the PID control system has a significant effect on the control performance. With the proportional control, it applies a corrective force that is proportional to the error state, and the proportional parameter is designed according to the error state. Moreover, the integral control can alleviate the steady-state error due to the load force,

and the integral parameter is selected based on the amount of the error state. In addition, the differential control is helpful for a faster system response and for the reduction of the tendency to overshoot, and the differential parameter is chosen in accordance with the derivative of the error state. In order to maintain the PID performance criteria, the corresponding fitness functions (performance criteria) in the proposed PSO-PID control scheme are defined as

$$f_p^j = 1 / [1 + (e_j)^2] \in [0, 1] \quad (17)$$

$$f_i^j = 1 / \left\{ 1 + \int_0^\infty [e_j(t)]^2 dt \right\} \in [0, 1] \quad (18)$$

$$f_d^j = 1 / [1 + (\dot{e}_j)^2] \in [0, 1] \quad (19)$$

where f_p^j , f_i^j , and f_d^j denote the j th ($j = 1, \dots, 5$) elements in the fitness function vectors, $\mathbf{f}_p = [f_p^1 \ f_p^2 \ f_p^3 \ f_p^4 \ f_p^5]^T \in R^{5 \times 1}$, $\mathbf{f}_i = [f_i^1 \ f_i^2 \ f_i^3 \ f_i^4 \ f_i^5]^T \in R^{5 \times 1}$, and $\mathbf{f}_d = [f_d^1 \ f_d^2 \ f_d^3 \ f_d^4 \ f_d^5]^T \in R^{5 \times 1}$, respectively. e_j is the j th element in the error state vector $\mathbf{e} \in R^{5 \times 1}$, and its derivative is expressed as \dot{e}_j . In (17)–(19), the superscript j in these fitness functions (f_p^j , f_i^j , and f_d^j) represents five different states including the central levitation height (z_O), rolling angle (θ), pitching angle (ϕ), bending angle (κ), and platform position (x_m) in the system. The j th elements of these fitness function vectors (\mathbf{f}_p , \mathbf{f}_i , and \mathbf{f}_d) are used to design the j th elements of the proportional, integral, and differential control vector (\mathbf{u}_p , \mathbf{u}_i , and \mathbf{u}_d) according to individual PSO processes, and each PSO process will possess individual global and local best particle by itself. To sum up, there are 15 particle groups in this case, and every PSO process will sort the particles that belong to a self group according to the individual fitness function. The functions of f_p^j , f_i^j , and f_d^j in (17)–(19) are all dependent on the error state e_j in evaluating the fitness level of the j th system state. Note that there are five independent states ($z_O, \theta, \phi, \kappa, x_m$) considered in the system position vector \mathbf{x} ; therefore, individual sequence elements in the fitness function vectors are independent. The basic PSO operations used in this paper are summarized as follows.

Global and Local Best Particle Decision: Initially, the particles forming the population should be randomly generated. After the fitness values of all the particles are calculated and sequenced, the particles with the first and second fitness values are, respectively, regarded as the global best ($g_{\text{best},p}^j$, $g_{\text{best},i}^j$, and $g_{\text{best},d}^j$) and local best ($l_{\text{best},p}^j$, $l_{\text{best},i}^j$, and $l_{\text{best},d}^j$) particle positions, in which $g_{\text{best},p}^j$, $g_{\text{best},i}^j$, and $g_{\text{best},d}^j$ are the j th elements in the global best vectors $\mathbf{g}_{\text{best},p} \in R^{5 \times 1}$, $\mathbf{g}_{\text{best},i} \in R^{5 \times 1}$, and $\mathbf{g}_{\text{best},d} \in R^{5 \times 1}$, respectively. $l_{\text{best},p}^j$, $l_{\text{best},i}^j$, and $l_{\text{best},d}^j$ are the j th elements in the local best vectors $\mathbf{l}_{\text{best},p} \in R^{5 \times 1}$, $\mathbf{l}_{\text{best},i} \in R^{5 \times 1}$, and $\mathbf{l}_{\text{best},d} \in R^{5 \times 1}$, respectively. Taking one PSO evolution for example, the global and local best particle positions will be applied to generate a new particle velocity. Then, the particle position is generated by using this new particle velocity. If the fitness value of the present particle position lies in between the fitness values of the local and global best particle position,

the present particle position will become the new local best particle position. If the fitness value of the present particle position is higher than the fitness values of the global best particle position, the present particle position will become the new global best particle position, and the old global best particle position will replace the local best particle position. If the fitness value of the present particle position is lower than the fitness value of the local best particle position, the local best particle position should be modified by

$$l_{\text{best},p}^j(n+1) = l_{\text{best},p}^j(n) + \delta_p^j \quad (20)$$

$$l_{\text{best},i}^j(n+1) = l_{\text{best},i}^j(n) + \delta_i^j \quad (21)$$

$$l_{\text{best},d}^j(n+1) = l_{\text{best},d}^j(n) + \delta_d^j \quad (22)$$

where n indicates the current state; $n+1$ means the next state; and δ_p^j , δ_i^j , and δ_d^j represent the j th ($j = 1, \dots, 5$) elements in the perturbation vectors $\delta_p \in R^{5 \times 1}$, $\delta_i \in R^{5 \times 1}$, and $\delta_d \in R^{5 \times 1}$, respectively. The perturbation vectors are designed as positive constants to prevent the local optimum problem [37].

Particle Velocity and Position: The PSO concept consists of, at each time step, changing the velocity of each particle toward its global and local best positions. The new velocities for each particle are updated by the following equations:

$$\begin{aligned} p_{v,p}^j(n+1) &= p_{v,p}^j(n) \times w_{v,p}^j \times e_j \\ &+ r_{1,p}^j \times [l_{\text{best},p}^j(n) - p_{p,p}^j(n)] \times e_j \\ &+ r_{2,p}^j \times [g_{\text{best},p}^j(n) - p_{p,p}^j(n)] \times e_j \end{aligned} \quad (23)$$

$$\begin{aligned} p_{v,i}^j(n+1) &= p_{v,i}^j(n) \times w_{v,i}^j \times \int_0^t e_j(\tau) d\tau \\ &+ r_{1,i}^j \times [l_{\text{best},i}^j(n) - p_{p,i}^j(n)] \times \int_0^t e_j(\tau) d\tau \\ &+ r_{2,i}^j \times [g_{\text{best},i}^j(n) - p_{p,i}^j(n)] \times \int_0^t e_j(\tau) d\tau \end{aligned} \quad (24)$$

$$\begin{aligned} p_{v,d}^j(n+1) &= p_{v,d}^j(n) \times w_{v,d}^j \times \dot{e}_j \\ &+ r_{1,d}^j \times [l_{\text{best},d}^j(n) - p_{p,d}^j(n)] \times \dot{e}_j \\ &+ r_{2,d}^j \times [g_{\text{best},d}^j(n) - p_{p,d}^j(n)] \times \dot{e}_j \end{aligned} \quad (25)$$

where $p_{p,p}^j$, $p_{p,i}^j$, and $p_{p,d}^j$ are the j th ($j = 1, \dots, 5$) elements in the particle position vectors $\mathbf{p}_{p,p} \in R^{5 \times 1}$, $\mathbf{p}_{p,i} \in R^{5 \times 1}$, and $\mathbf{p}_{p,d} \in R^{5 \times 1}$, respectively; $p_{v,p}^j$, $p_{v,i}^j$, and $p_{v,d}^j$ are the j th ($j = 1, \dots, 5$) elements in the velocity vectors $\mathbf{p}_{v,p} \in R^{5 \times 1}$, $\mathbf{p}_{v,i} \in R^{5 \times 1}$, and $\mathbf{p}_{v,d} \in R^{5 \times 1}$, respectively; $r_{1,p}^j$, $r_{1,i}^j$, and $r_{1,d}^j$ are the j th ($j = 1, \dots, 5$) elements in the local acceleration vectors $\mathbf{r}_{1,p} \in R^{5 \times 1}$, $\mathbf{r}_{1,i} \in R^{5 \times 1}$, and $\mathbf{r}_{1,d} \in R^{5 \times 1}$, respectively; $r_{2,p}^j$, $r_{2,i}^j$, and $r_{2,d}^j$ are the j th ($j = 1, \dots, 5$) elements in the global acceleration vectors $\mathbf{r}_{2,p} \in R^{5 \times 1}$, $\mathbf{r}_{2,i} \in R^{5 \times 1}$, and $\mathbf{r}_{2,d} \in R^{5 \times 1}$, respectively; and $w_{v,p}^j$, $w_{v,i}^j$, and $w_{v,d}^j$ denote the j th ($j = 1, \dots, 5$) elements in the inertial weight vectors

$w_{v,p} \in R^{5 \times 1}$, $w_{v,i} \in R^{5 \times 1}$, and $w_{v,d} \in R^{5 \times 1}$, respectively. This algorithm, by adjusting the inertial weight vectors, can accelerate the searching speed of the PSO control [20]–[22]. Because the particle velocities can be determined by (23)–(25), the new particle positions will be calculated at the next time step according to the following equations:

$$p_{p,p}^j(n+1) = p_{p,p}^j(n) \times w_{p,p}^j + p_{v,p}^j(n+1) \quad (26)$$

$$p_{p,i}^j(n+1) = p_{p,i}^j(n) \times w_{p,i}^j + p_{v,i}^j(n+1) \quad (27)$$

$$p_{p,d}^j(n+1) = p_{p,d}^j(n) \times w_{p,d}^j + p_{v,d}^j(n+1) \quad (28)$$

where $w_{p,p}^j$, $w_{p,i}^j$, and $w_{p,d}^j$ denote the j th ($j = 1, \dots, 5$) elements in the position-updating coefficient vectors $w_{p,p} \in R^{5 \times 1}$, $w_{p,i} \in R^{5 \times 1}$, and $w_{p,d} \in R^{5 \times 1}$, respectively, to reduce the convergent time [38]. However, the new particle positions will be set within the boundary region $[p_{p,p,\min}^j, p_{p,p,\max}^j]$, $[p_{p,i,\min}^j, p_{p,i,\max}^j]$, and $[p_{p,d,\min}^j, p_{p,d,\max}^j]$, in which $p_{p,p,\min}^j$, $p_{p,i,\min}^j$, and $p_{p,d,\min}^j$ are the j th elements in the minimum particle position vectors $p_{p,p,\min}$, $p_{p,i,\min}$, and $p_{p,d,\min}$, respectively; and $p_{p,p,\max}^j$, $p_{p,i,\max}^j$, and $p_{p,d,\max}^j$ are the j th elements in the maximum particle position vectors $p_{p,p,\max}$, $p_{p,i,\max}$, and $p_{p,d,\max}$, respectively.

For simplicity, the real-time PSO-PID control can be reorganized in the following vector form via (23)–(28):

$$\begin{aligned} u_{\text{pso}}(b_p, b_i, b_d) &= u_p + u_i + u_d \\ &= A_p E_p b_p + A_i E_i b_i + A_d E_d b_d \end{aligned} \quad (29)$$

where A_p , A_i , and A_d are known function matrices; E_p , E_i , and E_d are error function matrices; and b_p , b_i , and b_d are coefficient vectors to be adjusted. The detail elements in (29) are listed in Appendix D.

B. Lyapunov Stability Analyses

The proposed PSO-PID control scheme comprises three PID-type control parts and their associated evolutionary coefficients tuning algorithms. By way of imitation of the SM control law in (16) by the PSO algorithm, the coefficient adaptation laws for the PSO can be derived in the sense of Lyapunov stability theorem [32] to ensure a stable control performance. According to the powerful searching ability [18]–[22], there exists an optimal PSO control u_{pso}^* to learn the SM control law u_{SMC} such that

$$u_{\text{SMC}} = u_{\text{pso}}^*(b_p^*, b_i^*, b_d^*) + \varepsilon_{\text{pid}} \quad (30)$$

where ε_{pid} is a minimum reconstructed error vector and b_p^* , b_i^* , and b_d^* are the optimal parameters of b_p , b_i , and b_d in the PSO-PID control system, respectively. Design the PSO-PID control law as

$$u = \hat{u}_{\text{pso}}(\hat{b}_p, \hat{b}_i, \hat{b}_d) \quad (31)$$

where \hat{b}_p , \hat{b}_i , and \hat{b}_d are the estimates of b_p , b_i , and b_d , as adjusted by the adaptation laws that are to be introduced later.

Subtracting (31) from (30), an approximation error vector is defined as

$$\begin{aligned} \tilde{u} &= u_{\text{SMC}} - u = u_{\text{pso}}^* + \varepsilon_{\text{pid}} - \hat{u}_{\text{pso}} \\ &= A_p E_p \tilde{b}_p + A_i E_i \tilde{b}_i + A_d E_d \tilde{b}_d + \varepsilon_{\text{pid}} \end{aligned} \quad (32)$$

where $\tilde{b}_p = b_p^* - \hat{b}_p$, $\tilde{b}_i = b_i^* - \hat{b}_i$, and $\tilde{b}_d = b_d^* - \hat{b}_d$. Taking the summation of (11) and (16) and using (13), (15), and (32), one can obtain

$$G_s u_{\text{SMC}} = u_{\text{SMC}}^v + G_s u - M\ddot{x} - B\dot{x} - l_u \quad (33a)$$

$$\begin{aligned} G_s(u_{\text{SMC}} - u) &= M\ddot{e} + M\dot{L}\dot{e} + \dot{M}s_l/2 + K_s s_l \\ &\quad + \rho \text{sgn}(s_l) - l_u \end{aligned} \quad (33b)$$

$$\begin{aligned} M\dot{s}_l &= G_s A_p E_p \tilde{b}_p + G_s A_i E_i \tilde{b}_i + G_s A_d E_d \tilde{b}_d \\ &\quad + \psi_{\text{pid}} - \dot{M}s_l/2 - K_s s_l - \rho \text{sgn}(s_l) \end{aligned} \quad (33c)$$

where the uncertain term $\psi_{\text{pid}} = G_s \varepsilon_{\text{pid}} + l_u$ is also assumed to be bounded by $\|\psi_{\text{pid}}\|_1 < \rho$.

Theorem 1: Considering the dynamic model of a maglev transportation system including levitated electromagnets and a propulsive LIM represented by (11), if the PSO-PID control law is designed as (31) and the adaptation laws of the adjustable parameters are designed as (34a)–(34c), then the stability of the whole PSO-PID control scheme can be assured

$$\dot{\tilde{b}}_p^T = \eta_p (s_l^T G_s A_p E_p) \quad (34a)$$

$$\dot{\tilde{b}}_i^T = \eta_i (s_l^T G_s A_i E_i) \quad (34b)$$

$$\dot{\tilde{b}}_d^T = \eta_d (s_l^T G_s A_d E_d) \quad (34c)$$

where η_p , η_i , and η_d are positive learning rates.

Proof: Define a Lyapunov function candidate as

$$\begin{aligned} V(s_l(t), \tilde{b}_p, \tilde{b}_i, \tilde{b}_d) &= s_l^T M s_l/2 + \tilde{b}_p^T \tilde{b}_p/(2\eta_p) \\ &\quad + \tilde{b}_i^T \tilde{b}_i/(2\eta_i) + \tilde{b}_d^T \tilde{b}_d/(2\eta_d). \end{aligned} \quad (35)$$

Differentiating (35) and using (33), one can conclude that

$$\begin{aligned} \dot{V} &= s_l^T M \dot{s}_l + s_l^T \dot{M} s_l/2 - \dot{\tilde{b}}_p^T \tilde{b}_p/\eta_p - \dot{\tilde{b}}_i^T \tilde{b}_i/\eta_i - \dot{\tilde{b}}_d^T \tilde{b}_d/\eta_d \\ &= s_l^T \left[G_s A_p E_p \tilde{b}_p + G_s A_i E_i \tilde{b}_i + G_s A_d E_d \tilde{b}_d + \psi_{\text{pid}} \right. \\ &\quad \left. - \dot{M}s_l/2 - K_s s_l - \rho \text{sgn}(s_l) \right] + s_l^T \dot{M}s_l/2 \\ &\quad - \dot{\tilde{b}}_p^T \tilde{b}_p/\eta_p - \dot{\tilde{b}}_i^T \tilde{b}_i/\eta_i - \dot{\tilde{b}}_d^T \tilde{b}_d/\eta_d \\ &= -s_l^T K_s s_l + s_l^T \psi_{\text{pid}} - \|s_l^T\|_1 \rho \\ &\quad + \left(s_l^T G_s A_p E_p - \dot{\tilde{b}}_p^T/\eta_p \right) \tilde{b}_p \\ &\quad + \left(s_l^T G_s A_i E_i - \dot{\tilde{b}}_i^T/\eta_i \right) \tilde{b}_i \\ &\quad + \left(s_l^T G_s A_d E_d - \dot{\tilde{b}}_d^T/\eta_d \right) \tilde{b}_d. \end{aligned} \quad (36)$$

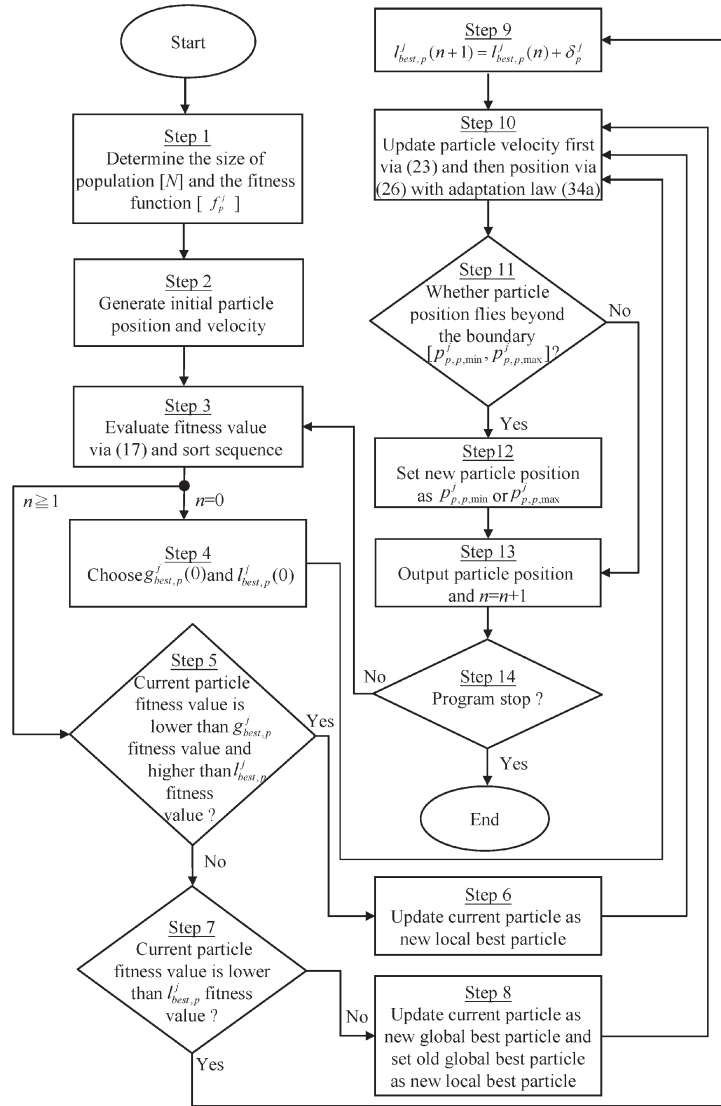


Fig. 3. Flowchart of the proportional control operation in the PSO-PID scheme.

If the adaptation laws for the adjustable coefficients in the PSO-PID control system are chosen as (34a)–(34c), (36) can be rewritten as

$$\begin{aligned}
 \dot{V} &= -s_l^T \mathbf{K}_s s_l + s_l^T \psi_{\text{pid}} - \|s_l^T\|_1 \rho \\
 &\leq -s_l^T \mathbf{K}_s s_l + \|s_l^T\|_1 \|\psi_{\text{pid}}\|_1 - \|s_l^T\|_1 \rho \\
 &= -s_l^T \mathbf{K}_s s_l - \|s_l^T\|_1 (\rho - \|\psi_{\text{pid}}\|_1) \\
 &\leq -s_l^T \mathbf{K}_s s_l \leq 0.
 \end{aligned} \tag{37}$$

Since $V(s_l(t), \tilde{b}_p, \tilde{b}_i, \tilde{b}_d) \leq 0$ is a negative semidefinite function (i.e., $V(s_l(t), \tilde{b}_p, \tilde{b}_i, \tilde{b}_d) \leq V(s_l(0), \tilde{b}_p, \tilde{b}_i, \tilde{b}_d)$), it implies that $s_l(t)$, \tilde{b}_p , \tilde{b}_i , and \tilde{b}_d are bounded functions. Let function $h(t) \equiv -s_l^T \mathbf{K}_s s_l \leq -\dot{V}(s_l(t), \tilde{b}_p, \tilde{b}_i, \tilde{b}_d)$, and integrate function $h(t)$ with respect to time

$$\int_0^t h(\tau) d\tau \leq V(s_l(0), \tilde{b}_p, \tilde{b}_i, \tilde{b}_d) - V(s_l(t), \tilde{b}_p, \tilde{b}_i, \tilde{b}_d). \tag{38}$$

Because $V(s_l(0), \tilde{b}_p, \tilde{b}_i, \tilde{b}_d)$ is bounded and $V(s_l(t), \tilde{b}_p, \tilde{b}_i, \tilde{b}_d)$ is nonincreasing and bounded function, the following result is obtained:

$$\lim_{t \rightarrow \infty} \int_0^t h(\tau) d\tau < \infty. \tag{39}$$

In addition, $\dot{h}(t)$ is bounded; therefore, by Barbalat's Lemma [32], one can conclude that $\lim_{t \rightarrow \infty} h(t) = 0$. This can imply that the sliding surface vector s_l go to zero asymptotically as time tends to become infinite. As a result, the stability of the proposed PSO-PID control system can be guaranteed. ■

In order to state the procedures involved in the design of the proposed PSO-PID control system clearly, the flowchart of the proportional control operation is shown in Fig. 3. To easily understand the PSO-PID control operation process, taking one PSO evolutionary mechanism that is used to obtain a proportional control effort of the central levitation height control, for example, it supposes that the four particle positions ($p_{p,p,1}^1, p_{p,p,2}^1, p_{p,p,3}^1, p_{p,p,4}^1$), as $j = 1$, and the corresponding

particle velocities ($p_{v,p,1}^1, p_{v,p,2}^1, p_{v,p,3}^1, p_{v,p,4}^1$) in the initial population ($N = 4$) are randomly chosen from the reasonable region $[p_{p,p,\min}^1, p_{p,p,\max}^1]$.

Process 1) In the first generation (Steps 1 and 2), the corresponding fitness values ($f_{p,1}^1, f_{p,2}^1, f_{p,3}^1, f_{p,4}^1$) are evaluated via immediate tracking responses (Step 3).

Process 2) By choosing the particle positions with the first and second fitness values from these four particles, the first fitness value is regarded as the global best particle position, and the second fitness value is utilized to be the local best particle position (Step 4).

Process 3) If the condition of $f_{p,3}^1 > f_{p,2}^1 > f_{p,4}^1 > f_{p,1}^1$ holds, then $p_{p,p,3}^1$ is chosen as the global best particle position ($g_{\text{best},p}^1(0)$), and $p_{p,p,4}^1$ is selected to be the local best particle position ($l_{\text{best},p}^1(0)$).

Process 4) After Process 3, it updates the particle velocity first via (23) and then the position via (26) (Step 10).

Process 5) If the new particle position flies beyond the boundary region $[p_{p,p,\min}^1, p_{p,p,\max}^1]$ (Step 11), the new particle position will be set as $p_{p,p,\min}^1$ or $p_{p,p,\max}^1$ (Step 12); else, it directly outputs the results of (26) as the new particle position (Step 13).

Process 6) After the first generation ($n \geq 1$), this new particle position will be treated as the current particle position of the next generation because it is the most suitable particle for the present circumstance.

Process 7) If the fitness value of the current particle position lies in between the fitness values of the global and local particle positions (Step 5), the current particle position will become the new local best particle position (Step 6).

Process 8) If the fitness value of the current particle position is higher than the global best fitness value, the current particle position will become the new global best particle position, and the old global best particle position will replace the local best particle position (Step 8).

Process 9) If the fitness value of the current particle position is lower than the local best fitness value (Step 7), the local best particle position should be modified by (20) (Step 9).

The operation process will repeat continuously until this program stops so that the suitable control current vector will be produced persistently. Consequently, the objective of real-time PSO-PID control can be achieved.

V. NUMERICAL SIMULATIONS AND EXPERIMENTAL RESULTS

In the levitation mechanism, EI-type (EI-96) electromagnets are adopted, and the coil turns for four electromagnets are all chosen as 230. The LIM used in the propulsive mechanism is a three-phase Y-connected two-pole 1.5-kW 60-Hz 110-V/10.2-A type. The detail parameters of the maglev transportation system [17] are listed as

$$l_t = w_t = 134 \text{ mm}$$

$$l_l = l_w = 33.5 \text{ mm}$$

$$z_{O,\max} = 5 \text{ mm}$$

$$M_{\text{lim}} = m_t = 14.6 \text{ kg}$$

$$D_{\text{lim}} = 113.56 \text{ kg/s}$$

$$K_f = 86 \text{ N/A} \quad (40)$$

where M_{lim} is the mover mass of the LIM and D_{lim} is the viscosity and iron-loss coefficient of the LIM. Numerical simulations of the control systems are implemented via the MATLAB software. Moreover, a second-order transfer function of the following form, with a rise time of 0.2 s, is chosen as the reference model, which is used to specify the reference trajectories for the levitation height of the maglev transportation system, for step commands

$$\frac{\omega_n^2}{s^2 + 2\zeta\omega_n s + \omega_n^2} = \frac{81}{s^2 + 18s + 81} \quad (41)$$

where s is the Laplace operator and ζ and ω_n are the damping ratio (set at one for critical damping) and undamped natural frequency, respectively. In addition, the mean-square-error (MSE) measures of position and angle responses are defined as

$$\text{MSE}(x_j) = \frac{1}{T} \sum_{z=1}^T e_j^2(z) \quad (42)$$

where x_j and e_j indicate the elements of the system position vector $x = [z_O \ \theta \ \phi \ \kappa \ x_m]^T$ and the corresponding error state vector e and T is the total sampling instants. According to (42), the normalized-MSE (NMSE) values of the levitation-height response, angle response, and platform-position response using per-unit values with a 10^{-6} – mm, 10^{-6} – degree, and 10^{-4} – cm bases are used in examining the control performance in this paper. In order to exhibit the superiority of the proposed PSO-PID control scheme, a PID control presented in [28] is also adopted to control the maglev transportation system. In this PSO-PID control scheme, five PID controllers are designed by using $f^j(e_j) = \exp(-e_j^2)|_{j=1,\dots,5}$ as individual fitness functions to produce suitable control currents, and their proportional, integral, and differential control gains are determined by the PSO algorithm offline.

A. Numerical Simulations

To investigate the robustness of the proposed control systems, the following two cases with parameter variations and time-varying external force disturbance are considered.

Case 1) A step command for the central levitation height is set at $z_{Od} = 1$ mm initially, and a sinusoidal command for the platform position is chosen as $x_{md} = 10 \sin[0.2\pi(t-1)]$ cm after 1 s. An additional weight of 0.5 kg is loaded on c_C at 2 s and is unloaded at 5 s.

Case 2) A step command for the central levitation height is set at $z_{Od} = 0.5$ mm initially and is changed from 0.5 to 2 mm at 4 s and from 2 to 1 mm at 6 s. A sinusoidal command for the platform position is chosen as $x_{md} = 10 \sin(0.2\pi t)$ cm. An additional weight of 1 kg is loaded on c_O at 2 s and is unloaded at 5 s.

Other identical conditions in these two cases are represented as the following: 1) initial system state: $z_O(0) = 0.2$ mm, $\theta(0) = 0^\circ$, $\phi(0) = 0^\circ$, and $x_m(0) = 0$ cm; 2) external force disturbance occurring at 7 s: $\mathbf{f}_{d0} = [2\pi \sin(2\pi t) \sin(2\pi t) \cos(2\pi t) - (\cos(2\pi t)/M_{lim})l_t \sin(\phi) \ 0 \ (\cos(2\pi t)/M_{lim})]^T$; and 3) parameter variations: $K_f \propto 1/[z_O(t) - z_O(0)]^2$ and $D_{lim} \propto 1/[z_O(t) - z_O(0)]^2$. Moreover, the control parameters of the SM and PSO-PID control systems are given as

$$\begin{aligned} \mathbf{L} &= \text{diag}(320, 100, 80, 100, 200) \quad \rho = 50 \quad N = 4 \\ \eta_p &= 4.5 \quad \eta_i = 3.2 \quad \eta_d = 2.6 \\ \mathbf{K}_s &= \text{diag}(100, 10, 10, 10, 10) \\ \delta_p &= [50, 40, 43, 0.5, 80]^T \quad \delta_i = [50, 40, 43, 0.5, 50]^T \\ \delta_d &= [80, 58, 48, 0.5, 65]^T \quad \mathbf{p}_{p,p,\min} = [0, 0, 0, 0, 0]^T \\ \mathbf{p}_{p,p,\max} &= [24\ 298, 4283, 4174, 8780, 1221]^T \\ \mathbf{p}_{p,i,\min} &= [0, 0, 0, 0, 0]^T \quad \mathbf{p}_{p,d,\min} = [0, 0, 0, 0, 0]^T \\ \mathbf{p}_{p,i,\max} &= [457\ 184, 48\ 344, 28\ 317, 146\ 555, 1837]^T \\ \mathbf{p}_{p,d,\max} &= [20\ 139, 287, 367, 1289, 254]^T. \end{aligned} \quad (43)$$

Note that \mathbf{L} and \mathbf{K}_s are chosen to achieve the best transient control performance in numerical simulations and experimental results by considering the requirement of stability and the possible operating conditions. The choices of the perturbation vectors δ_p , δ_i , and δ_d have relations with the ability to move out from local optimum. The boundary regions of particle position vectors ($\mathbf{p}_{p,p,\min}$, $\mathbf{p}_{p,p,\max}$, $\mathbf{p}_{p,i,\min}$, $\mathbf{p}_{p,i,\max}$, $\mathbf{p}_{p,d,\min}$, and $\mathbf{p}_{p,d,\max}$) are decided by allowable ranges of control gains for practical applications. The bound (ρ) of the lumped uncertainty vector can be determined roughly owing to the limitation of the control effort and the possible perturbed range of parameter variations and external disturbance. The choice of population (N) could be designed with a large size for large-scale searching. According to (D3a)–(D3c), it is obvious that the inertial weight vectors and the position-updating coefficient vectors are automatically adjusted via the adaptation laws in (34a)–(34c). In this paper, the control objective is to make the central levitation height and moving position of the platform follow reference trajectories and to keep the corresponding rolling and pitching angles horizontal (i.e., $\theta_d = \phi_d = \kappa_d = 0$) under the possible occurrence of uncertainties. All of the illustrations of the PSO-PID in [28], SM, and proposed PSO-PID control systems are shown in Figs. 4–6, respectively, where (a)–(c) and (g)–(i) are the tracking responses of the central levitation height and rolling and pitching angles at cases 1 and 2, respectively; (d) and (j) are the tracking responses of the platform position at cases 1 and 2, respectively; (e) and (k) are the related attitude control forces at cases 1 and 2, respectively; and (f) and (l) are the LIM force control currents at cases 1 and 2, respectively.

Fig. 4 shows the simulated results of the PSO-PID strategy proposed by Gaing [28] at cases 1 and 2. As can be seen from this figure, there are apparent errors under the occurrence of system uncertainties because these control gains in the PID controllers are determined offline. Although this problem could be improved by retuning these control gains, it is time-

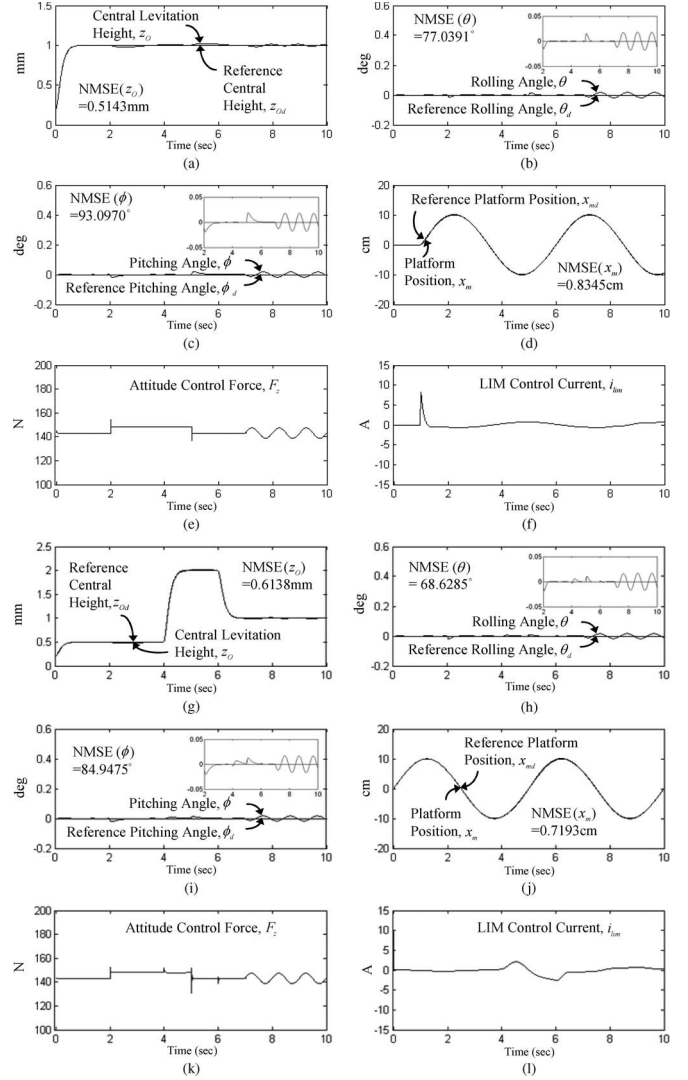


Fig. 4. Numerical simulations of the PSO-PID control in [28]. (a)–(f) At case 1. (g)–(l) At case 2.

consuming and laborious. Fig. 5 shows the simulated results of the SM control strategy presented in Section III at cases 1 and 2. In Fig. 5(a) and (g), the central levitation heights follow the reference trajectories well before 2 s, but the performances become little shaking because of the additional weight loading and unloading as 2 and 5 s and external force disturbance occurring at 7 s. Similarly, the degenerate rolling and pitching angles in Fig. 5(b), (c), (h), and (i) that are caused by the inappropriate selection of ρ also occurred after 2 s. In addition, the tracking responses of the platform position in Fig. 5(d) and (j) seem to be less sensitive to the occurrence of uncertainties than the central levitation height because of a large travel distance. Unfortunately, the chattering phenomena in the control efforts, which are shown in Fig. 5(e), (k), (f) and (l), are serious. Although a smaller bound of the lumped uncertainty vector can solve the problem of chattering phenomena, it will result in poor tracking responses.

For comparison, the proposed PSO-PID control system is also applied to control the maglev transportation system. By considering the same simulated cases as the PSO-PID in [28] and SM control strategies, the simulated results of the proposed

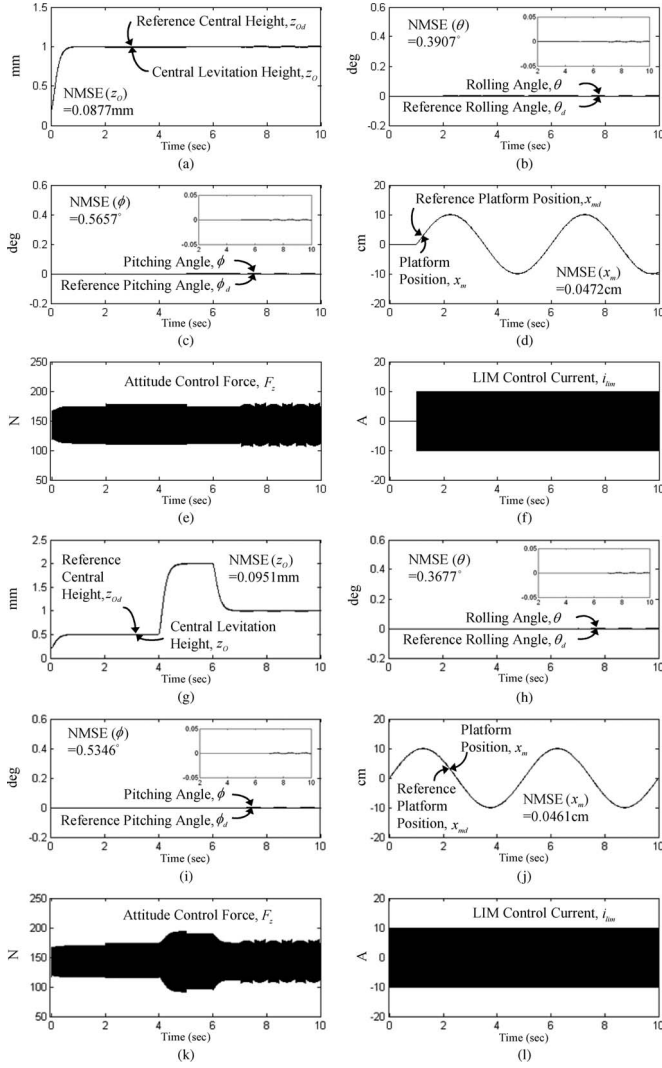


Fig. 5. Numerical simulations of the SM control strategy. (a)–(f) At case 1. (g)–(l) At case 2.

PSO-PID control system at cases 1 and 2 are shown in Fig. 6. As can be seen from Fig. 6(a)–(d) and (g)–(j), the error state vector converges quickly, and the robust control characteristics under the occurrence of varied reference trajectories, parameter variations, and external force disturbance can be clearly observed. By observing Fig. 6(e), (f), (k), and (l), undesirable chattering phenomena of the SM control strategy, as shown in Fig. 5(e), (f), (k), and (l), can be removed. Note that there are shaking control efforts at the later response because of the external force disturbance, with the sine or cosine shape occurring at 7 s.

B. Experimental Results

In this paper, the image of the experimental equipment for the maglev transportation system is shown in Fig. 7, and it can be divided into levitation and propulsion mechanisms. In the levitation mechanism, four EI-type (EI-96) electromagnets are adopted, and the coil turns for four electromagnets are all chosen as 230. These electromagnets are excited by Kollmorgen dc linear servo amplifiers with current mode control (EM 19-28030-B00). Moreover, the corresponding levitation heights are

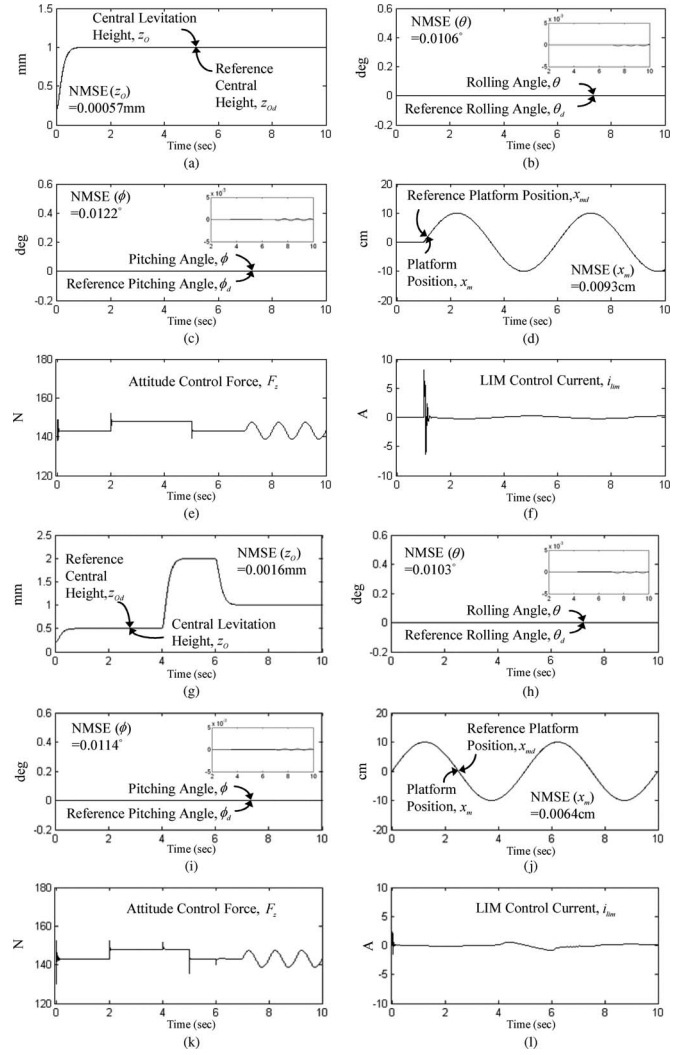


Fig. 6. Numerical simulations of the proposed PSO-PID control strategy. (a)–(f) At case 1. (g)–(l) At case 2.

measured via analog inductive gap sensors (IAS-10-A13-IL) installed in the location of individual mass center. In the propulsion mechanism, the adopted LIM is a three-phase Y-connected two-pole 1.5-kW 60-Hz 110-V/10.2-A type and is driven by a current-controlled pulsewidth-modulation (PWM) voltage source inverter. It is implemented by an intelligent-power-module power component (CM75TF-12H) manufactured by Mitsubishi Co. with a switching frequency of 15 kHz. In the Hall current sensor, the amplifier rate is 0.8, and the relationship between the current and the voltage is 18.75 such that the entire amplification factor is 15. The delay time is decided by the user but with a least demand for 2 μ s. In addition, the corresponding displacement in the propulsion mechanism is measured by a magnetic sensor (SMK-L-1-10-I-2) with a magnetic tape. As the magnetic sensor is moved along the magnetic tape, it detects the displacement and produces an output signal equivalent to that of an incremental encoder.

In order to present the value of the proposed control systems in practical applications, a digital-signal-processor (DSP)-based control platform is used for the maglev transportation system. All experimental computer programs are carried out using Turbo C language inserted into a DSP development

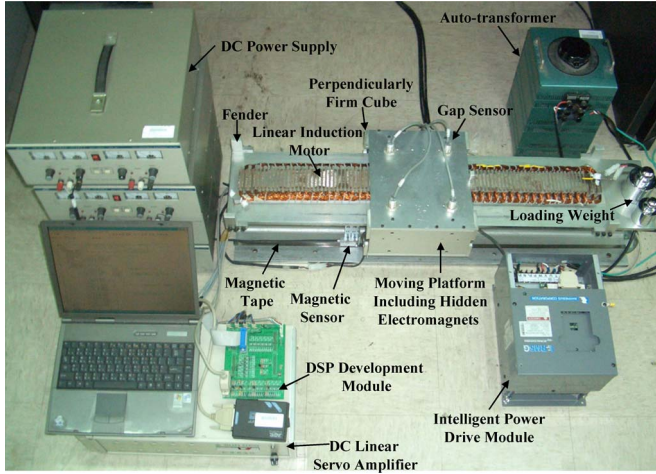


Fig. 7. Image of the experimental equipment.

module. This development module has a Texas Instruments TMS320LF2407AEVM central processing unit, 16 channel 10-bit analog-to-digital and 4 channel 12-bit digital-to-analog converters, and a digital port. The central processing unit has a 40MIPS 16-bit fixed point DSP core, 2 PWM channels with 15 kHz, 4 timer channels, and 2 encoder channels. Moreover, there are interface circuits for command and data communication between the computer and the development module. In practical applications, the propulsion force of the LIM will be weakened due to the increase of levitation height. According to allowable levitation regions (from $z_{O,\min} = 0.2$ mm to $z_{O,\max} = 5$ mm), a step command for the central levitation height is set at $z_{Od} = 1$ mm in the experiments. In addition, an additional weight of 1 kg on the mass center of the moving platform (c_O) (Condition 1) or the mass center of the subplatform C (c_C) (Condition 2) is loaded at 6 s and is unloaded at 12 s.

All of the experiments of the PSO-PID in [28], SM, and proposed PSO-PID control systems are shown in Figs. 8–10, respectively, where (a)–(c) and (g)–(i) are the tracking responses of the central levitation height and rolling and pitching angles under loading and unloading an additional weight on c_O and c_C , respectively; (d) and (j) are the tracking responses of the platform position under loading and unloading an additional weight on c_O and c_C , respectively; (e) and (k) are the related attitude control forces under loading and unloading an additional weight on c_O and c_C , respectively; and (f) and (l) are the LIM force control currents under loading and unloading an additional weight on c_O and c_C , respectively.

The experimental results of the PSO-PID control scheme proposed by Gaing [28] at $z_{Od} = 1$ mm and $\theta_d = \phi_d = 0$ are shown in Fig. 8. Owing to the absence of the damping or restricting force on the moving platform, the overshoot to the command step and oscillation transient responses occur. The central levitation height can follow the reference trajectory at about 2 s, but the performances become poor because of the additional weight loading and unloading as 6 and 12 s. Similarly, the degenerate rolling and pitching angles are affected simultaneously. Because proportional, integral, and differential control gains are determined by the PSO algorithm offline,

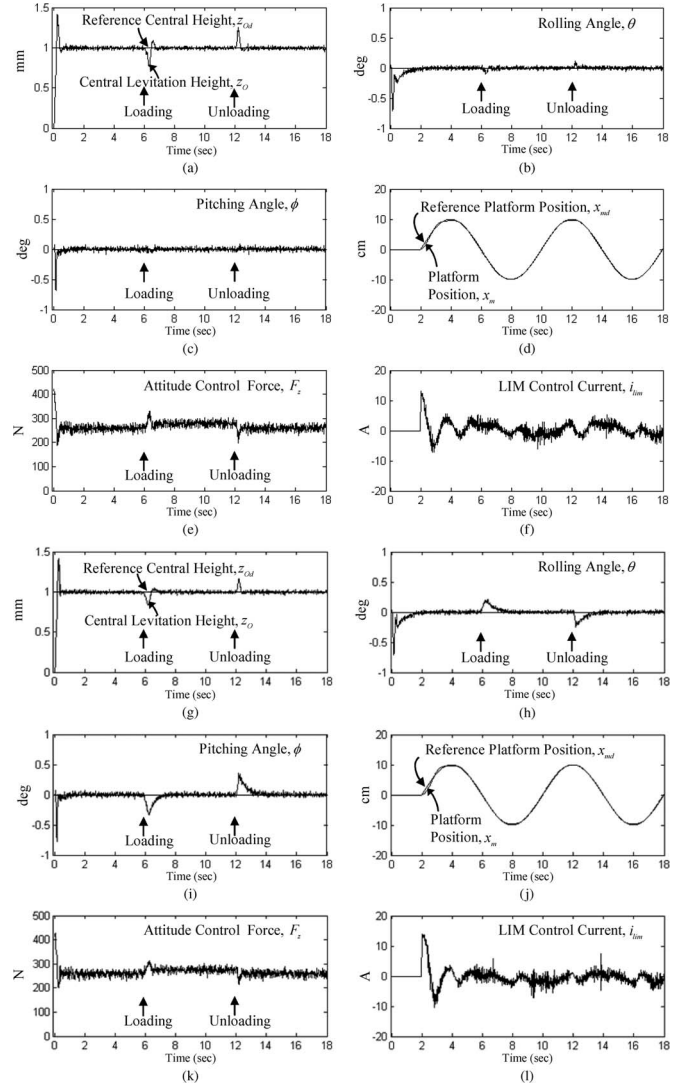


Fig. 8. Tracking response of the central levitation height, rolling and pitching angle responses, platform position response, attitude control force, and LIM force control current of the PSO-PID control in [28] at $z_{Od} = 1$ mm and $\theta_d = \phi_d = 0$. (a)–(f) Condition 1. (g)–(l) Condition 2.

the fixed-gain PSO-PID controllers are not robust to wide parameter variations and large external disturbances.

The tracking response of central levitation height, rolling and pitching angle responses, platform position response, attitude control force, and LIM force control current of the SM control system presented in Section III at $z_{Od} = 1$ mm and $\theta_d = \phi_d = 0$ are shown in Fig. 9. From the experimental results, the chattering phenomena of the control efforts result in shaking tracking responses, and the degenerate rolling and pitching angle responses after 6 s are caused by the inappropriate selection of ρ . Although this problem could be solved by selecting a larger bound of the lumped uncertainty vector, it will result in more serious chattering and excessive control currents. Moreover, the undesired chattering control efforts will wear the mechanical structure and might excite unstable system dynamics. The corresponding experimental verifications of the proposed PSO-PID control system are given in Fig. 10. As can be seen from Fig. 10(a)–(d) and (g)–(j), the robust tracking and balancing control characteristics under the occurrence of

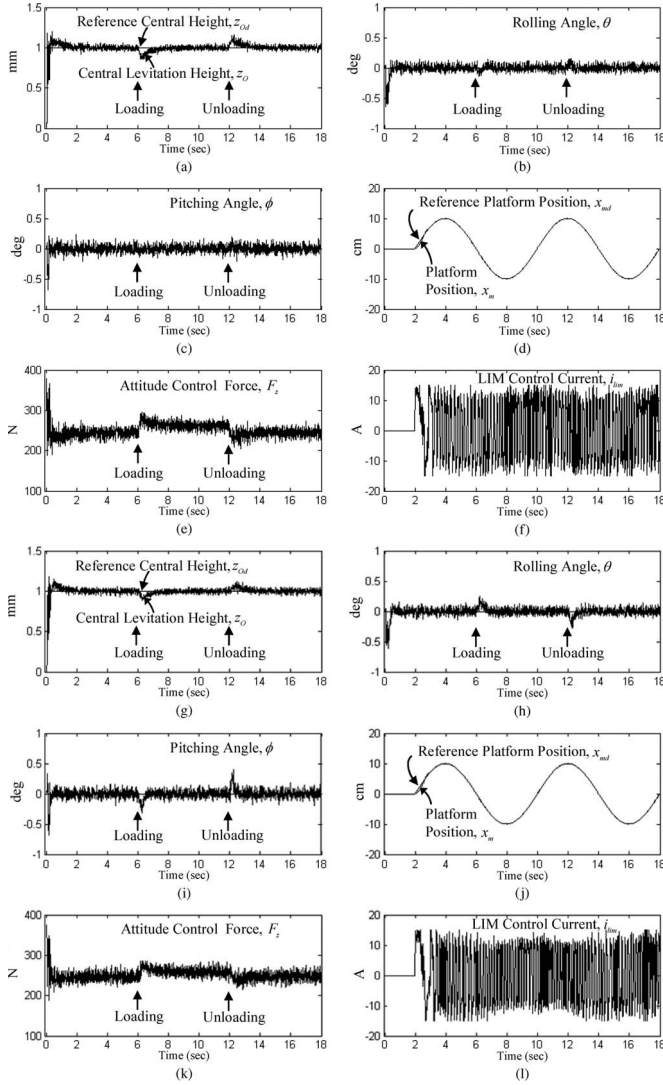


Fig. 9. Tracking response of the central levitation height, rolling and pitching angle responses, platform position response, attitude control force, and LIM force control current of the SM control system at $z_{Od} = 1$ mm and $\theta_d = \phi_d = 0$. (a)–(f) Condition 1. (g)–(l) Condition 2.

the additional weight can be clearly observed. By observing Fig. 10(e), (f) (k), and (l), the undesirable chattering phenomena of the SM control strategy, as shown in Fig. 9(e), (f), (k), and (l), can be greatly alleviated. Basically, these experimental results shown in Figs. 8–10 agree with the numerical simulations given in Figs. 4–6. The tracking and balancing control performance of the proposed PSO-PID control scheme is excellent whether in the simulation or in the experimentation.

VI. CONCLUSION

This paper has successfully investigated the online PSO-PID control scheme for the levitated and propulsive control of the maglev transportation system. The proposed PSO-PID control system has the salient merits of real-time control design, control effort without chattering in comparison with the SM control, and favorable robust characteristic in comparison with the fixed-gain PID control. Moreover, the simulated and experimental comparisons of the PSO-PID in [28], SM, and

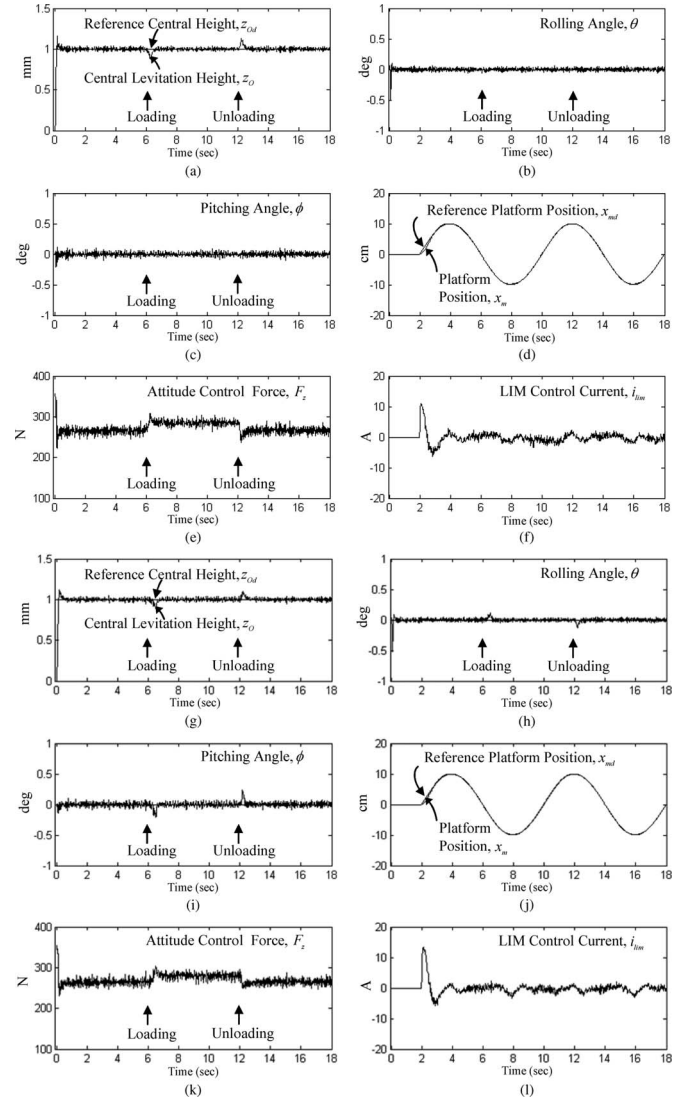


Fig. 10. Tracking response of the central levitation height, rolling and pitching angle responses, platform position response, attitude control force, and LIM force control current of the proposed PSO-PID control system at $z_{Od} = 1$ mm and $\theta_d = \phi_d = 0$. (a)–(f) Condition 1. (g)–(l) Condition 2.

proposed PSO-PID control systems are summarized in Tables I and II, respectively. According to the NMSE measures, the proposed PSO-PID control scheme has over 99.74% and 98.32% height-tracking improvements, 99.98% and 97.20% angle-stabilizing improvements, and 98.89% and 80.30% position-tracking improvements in numerical simulations and has over 87.14% and 78.0% height-tracking improvements, 87.36% and 73.6% angle-stabilizing improvements, and 82.31% and 49.14% position-tracking improvements in experimental results than the PSO-PID in [28] and SM control strategies, respectively. Consequently, the proposed PSO-PID control system indeed yields a superior performance than the PSO-PID in [28] and SM control strategies.

The major achievements of this paper are the following. 1) The successful construction of the mathematical model of a maglev transportation system including levitated electromagnets and a propulsive LIM based on the concepts of mechanical geometry and motion dynamics. 2) The successful utilization of PSO with PID-type as the major control role to recast its

TABLE I
SIMULATED PERFORMANCE COMPARISONS OF PSO-PID IN [28], SM, AND PROPOSED PSO-PID CONTROL SYSTEMS

Control Systems Performance	PSO-PID Control in [28]		SM Control		Proposed PSO-PID Control	
	Case 1	Case 2	Case 1	Case 2	Case 1	Case 2
NMSE(z_o)	0.5143mm	0.6138mm	0.0877mm	0.0951mm	0.00057mm	0.0016mm
NMSE(θ)	77.0391°	68.6285°	0.3907°	0.3677°	0.0106°	0.0103°
NMSE(ϕ)	93.0970°	84.9475°	0.5657°	0.5346°	0.0122°	0.0114°
NMSE(x_m)	0.8345cm	0.7193cm	0.0472cm	0.0461cm	0.0093cm	0.0064cm

TABLE II
EXPERIMENTAL PERFORMANCE COMPARISONS OF PSO-PID IN [28], SM, AND PROPOSED PSO-PID CONTROL SYSTEMS

Control Systems Performance	PSO-PID Control in [28]		SM Control		Proposed PSO-PID Control	
	Condition 1	Condition 2	Condition 1	Condition 2	Condition 1	Condition 2
NMSE(z_o)	76.231mm	108.863mm	44.547mm	82.121mm	9.802mm	10.033mm
NMSE(θ)	132.124°	184.369°	61.977°	83.075°	13.491°	17.148°
NMSE(ϕ)	162.787°	196.829°	77.959°	102.621°	20.580°	22.075°
NMSE(x_m)	40.776cm	44.113cm	14.772cm	15.343cm	4.158cm	7.803cm

traditional idea of minor compensatory function in previous researches. 3) The successful derivation of adaptation laws by Lyapunov stability analyses to decide appropriate evolutionary coefficients in the real-time PSO control operation. 4) The successful guarantee of the system stability for the proposed PSO-PID control system without the requirement of auxiliary compensated controllers, strict constraints, and control transformations. 5) The successful application and comparison of three different controllers (PSO-PID in [28], SM, and PSO-PID control) for a maglev transportation system to demonstrate the value of using the proposed PSO-PID approach over fixed-gain PSO-PID and SM control.

APPENDIX A

In the 3-D coordinate system as shown in Fig. 1(b), three DOF of the moving platform, including z_o , θ , and ϕ , are considered in analyzing the dynamic model in this paper. After mathematical manipulations, the kinetic energy E_p of the moving platform can be represented as

$$E_p = 0.5m_t\dot{z}_o^2 + 0.5I_x\dot{\theta}^2 + 0.5I_y\dot{\phi}^2 \quad (A1)$$

where m_t is the total mass of the moving platform and $I_x = m_t w_t^2/12$ and $I_y = m_t l_t^2/12$ are the inertia with respect to the

x - and y -axes, respectively [39]. Moreover, the potential energy U_p of the moving platform can be expressed as

$$U_p = m_t g z_o \quad (A2)$$

where g is the gravity acceleration. Thus, the Lagrange equations of motion are

$$\begin{aligned} \frac{d}{dt} \left(\frac{\partial L}{\partial \dot{z}_o} \right) - \frac{\partial L}{\partial z_o} &= F_z & \frac{d}{dt} \left(\frac{\partial L}{\partial \dot{\theta}} \right) - \frac{\partial L}{\partial \theta} &= T_\theta \\ \frac{d}{dt} \left(\frac{\partial L}{\partial \dot{\phi}} \right) - \frac{\partial L}{\partial \phi} &= T_\phi \end{aligned} \quad (A3)$$

where L is Lagrangian and is defined as the total kinetic energy minus the potential energy

$$L \equiv E_p - U_p. \quad (A4)$$

According to (A1)–(A4), the dynamic equations of the maglev system can be expressed as

$$m_t \ddot{z}_o + m_t g = F_z \quad (A5)$$

$$I_x \ddot{\theta} = T_\theta \quad (A6)$$

$$I_y \ddot{\phi} = T_\phi. \quad (A7)$$

The dynamic motions in (A5)–(A7) are similar to the results derived from the Newton's second law of motion [40]. A general differential equation representing the rigidity of the platform can be represented as

$$\ddot{\kappa} = -\alpha\dot{\kappa} + T_\kappa \quad (\text{A8})$$

where α is a positive coefficient and $T_\kappa = l_d(f_A - f_B - f_C + f_D)$, with $l_d = \sqrt{l_w^2 + l_l^2}$. The bending angle κ is a constant value so that the condition of $T_\kappa = l_d(f_A - f_B - f_C + f_D) = 0$ always holds because the moving platform is assumed to be a rigid body. In addition, the vector $\mathbf{f}_{pl} = [F_z \ T_\theta \ T_\phi \ T_\kappa \ F_{lim}]^T$ of the moving platform can be obtained by

$$\begin{aligned} \mathbf{f}_{pl} &= \mathbf{G}_p \mathbf{f} = \mathbf{\Lambda}_l \mathbf{G}_s \mathbf{f} = \mathbf{\Lambda}_l \mathbf{G}_s \mathbf{\Lambda}_g \mathbf{u} = \mathbf{\Lambda}_l \mathbf{G}_s \mathbf{\Lambda}_g \mathbf{I}_5 \mathbf{u} \\ &= \mathbf{\Lambda}_l \mathbf{G}_s \mathbf{\Lambda}_g (\mathbf{G}_s^T \mathbf{\Lambda}_N \mathbf{\Lambda}_N \mathbf{G}_s) \mathbf{u} = \mathbf{G}_g \mathbf{G}_s \mathbf{u} = \mathbf{u}_c \end{aligned} \quad (\text{A9})$$

$$\text{where } \mathbf{G}_p = \begin{bmatrix} 1 & 1 & 1 & 1 & 0 \\ -l_w & l_w & -l_w & l_w & 0 \\ -l_l & -l_l & l_l & l_l & 0 \\ l_d & -l_d & -l_d & l_d & 0 \\ 0 & 0 & 0 & 0 & 1 \end{bmatrix} = \mathbf{\Lambda}_l \mathbf{G}_s, \quad \text{with}$$

$$\mathbf{\Lambda}_l = \text{diag}[1, l_w, l_l, l_d, 1] \text{ and } \mathbf{G}_s = \begin{bmatrix} 1 & 1 & 1 & 1 & 0 \\ -1 & 1 & -1 & 1 & 0 \\ -1 & -1 & 1 & 1 & 0 \\ 1 & -1 & -1 & 1 & 0 \\ 0 & 0 & 0 & 0 & 1 \end{bmatrix},$$

and $\mathbf{\Lambda}_g = \text{diag}[G_A, G_B, G_C, G_D, K_f]$ with which the applied control force vector $\mathbf{f} = [f_A \ f_B \ f_C \ f_D \ F_{lim}]^T$ can be expressed as $\mathbf{f} = \mathbf{\Lambda}_g \mathbf{u}$ in terms of the control current vector $\mathbf{u} = [i_A^2 \ i_B^2 \ i_C^2 \ i_D^2 \ i_{lim}]^T$. It is easily verified that $\mathbf{G}_s^T \mathbf{G}_s = \begin{bmatrix} 4\mathbf{I}_4 & 0 \\ 0 & 1 \end{bmatrix}$ holds. Therefore, one can write $\mathbf{G}_s^T \mathbf{\Lambda}_N \mathbf{\Lambda}_N \mathbf{G}_s = \begin{bmatrix} \mathbf{I}_4 & 0 \\ 0 & 1 \end{bmatrix} = \mathbf{I}_5$, where $\mathbf{\Lambda}_N = \begin{bmatrix} 0.5\mathbf{I}_4 & 0 \\ 0 & 1 \end{bmatrix}$, and also $\mathbf{G}_s^T \mathbf{\Lambda}_N = (\mathbf{\Lambda}_N \mathbf{G}_s)^T = (\mathbf{\Lambda}_N \mathbf{G}_s)^{-1}$. \mathbf{G}_s is therefore invertible.

APPENDIX B

In general, the mechanical equation of a LIM can be denoted as [4], [5]

$$M_{lim} \ddot{x}_m + D_{lim} \dot{x}_m + F_l = F_{lim} \quad (\text{B1})$$

where M_{lim} is the mover mass of the LIM, D_{lim} is the viscosity and iron-loss coefficient, x_m is the platform position, F_{lim} denotes the propulsive force, and F_l represents the external force disturbance, the unstructured mutual force reaction between the electromagnets and the LIM, and the unpredictable uncertainties. With suitable impressed current or field-oriented control [4], the propulsive force can be simplified as

$$F_{lim} = K_f i_{lim} \quad (\text{B2})$$

where K_f is the LIM force constant and i_{lim} is the LIM force control current. According to (B1) and (B2), the dynamic model

of the propulsive LIM in the maglev transportation system can be reformulated as

$$M_{lim} \ddot{x}_m + D_{lim} \dot{x}_m = K_f i_{lim} - F_l. \quad (\text{B3})$$

APPENDIX C

The mass and inertia matrix $\mathbf{M}_0 \in R^{5 \times 5}$ in (6) is a positive-definite matrix and is defined as

$$\mathbf{M}_0 = \text{diag}[m_t, I_x, I_y, 1, M_{lim}]. \quad (\text{C1})$$

According to (7) and Appendix B, the inverse matrix of \mathbf{G}_g can be denoted as

$$\mathbf{G}_g^{-1} = \mathbf{\Lambda}_N^{-2} \mathbf{G}_s^{-T} \mathbf{\Lambda}_g^{-1} \mathbf{G}_s^{-1} \mathbf{\Lambda}_l^{-1}. \quad (\text{C2})$$

The diagonal matrices $\mathbf{\Lambda}_l$, $\mathbf{\Lambda}_g$, and $\mathbf{\Lambda}_N$ are positive definite. Therefore, the symmetric matrix $\mathbf{G}_a = \mathbf{G}_s \mathbf{\Lambda}_g \mathbf{G}_s^T$ and also all nonsymmetric matrices $\mathbf{\Lambda}_l \mathbf{G}_a$, $\mathbf{G}_a \mathbf{\Lambda}_N^2$, and $\mathbf{G}_g = \mathbf{\Lambda}_l \mathbf{G}_a \mathbf{\Lambda}_N^2$ are each positive definite. Since $\mathbf{G}_g = \mathbf{\Lambda}_l \mathbf{G}_s \mathbf{\Lambda}_g \mathbf{G}_s^T \mathbf{\Lambda}_N^2$ is positive definite, it is invertible, and the inverse is inherently positive definite. Therefore, the dynamic model (8) is obtained by means of $\mathbf{B} = \mathbf{G}_g^{-1} \mathbf{B}_0$, $\mathbf{d} = \mathbf{G}_g^{-1} \mathbf{d}_0$, and $\mathbf{M} = \mathbf{G}_g^{-1} \mathbf{M}_0$. Note that the property of a positive-definite matrix $\mathbf{M} = \mathbf{G}_g^{-1} \mathbf{M}_0$ is verified by the fact that the product of two positive-definite matrices in (C1) and (C2) is also positive definite. Moreover, the viscosity matrix $\mathbf{B}_0 \in R^{5 \times 5}$ in (6) is defined as

$$\mathbf{B}_0 = \text{diag}[0, 0, 0, 0, D_{lim}]. \quad (\text{C3})$$

In addition, the gravity vector $\mathbf{d}_0 \in R^{5 \times 1}$ in (6) is given as

$$\mathbf{d}_0 = [m_t g \ 0 \ 0 \ 0 \ 0]^T. \quad (\text{C4})$$

APPENDIX D

The matrices $\mathbf{A}_p \in R^{5 \times 20}$, $\mathbf{A}_i \in R^{5 \times 20}$, and $\mathbf{A}_d \in R^{5 \times 20}$ in (29) are defined as

$$\mathbf{A}_p = \text{diag}[\mathbf{a}_{p,j}] \text{ with}$$

$$\begin{aligned} \mathbf{a}_{p,j} &= \begin{bmatrix} p_{p,p}^j & p_{v,p}^j \end{bmatrix} \begin{bmatrix} l_{best,p}^j - p_{p,p}^j \\ g_{best,p}^j - p_{p,p}^j \end{bmatrix}, \\ j &= 1, \dots, 5 \end{aligned} \quad (\text{D1a})$$

$$\mathbf{A}_i = \text{diag}[\mathbf{a}_{i,j}] \text{ with}$$

$$\begin{aligned} \mathbf{a}_{i,j} &= \begin{bmatrix} p_{p,i}^j & p_{v,i}^j \end{bmatrix} \begin{bmatrix} l_{best,i}^j - p_{p,i}^j \\ g_{best,i}^j - p_{p,i}^j \end{bmatrix}, \\ j &= 1, \dots, 5 \end{aligned} \quad (\text{D1b})$$

$$\mathbf{A}_d = \text{diag}[\mathbf{a}_{d,j}] \text{ with}$$

$$\begin{aligned} \mathbf{a}_{d,j} &= \begin{bmatrix} p_{p,d}^j & p_{v,d}^j \end{bmatrix} \begin{bmatrix} l_{best,d}^j - p_{p,d}^j \\ g_{best,d}^j - p_{p,d}^j \end{bmatrix}, \\ j &= 1, \dots, 5. \end{aligned} \quad (\text{D1c})$$

Moreover, the matrices $\mathbf{E}_p \in R^{20 \times 20}$, $\mathbf{E}_i \in R^{20 \times 20}$, and $\mathbf{E}_d \in R^{20 \times 20}$ in (29) are expressed as

$$\mathbf{E}_p = \text{diag}[\mathbf{E}_{p,j}] \text{ with } \mathbf{E}_{p,j} = \text{diag}[1, e_j, e_j, e_j], \quad j = 1, \dots, 5 \quad (\text{D2a})$$

$$\mathbf{E}_i = \text{diag}[\mathbf{E}_{i,j}] \text{ with } \mathbf{E}_{i,j} = \text{diag} \left[1, \int_0^t e_j(\tau) d\tau, \int_0^t e_j(\tau) d\tau, \int_0^t e_j(\tau) d\tau \right], \quad j = 1, \dots, 5 \quad (\text{D2b})$$

$$\mathbf{E}_d = \text{diag}[\mathbf{E}_{d,j}] \text{ with } \text{diag}[1, \dot{e}_j, \dot{e}_j, \dot{e}_j], \quad j = 1, \dots, 5. \quad (\text{D2c})$$

In addition, the vectors $\mathbf{b}_p \in R^{20 \times 1}$, $\mathbf{b}_i \in R^{20 \times 1}$, and $\mathbf{b}_d \in R^{20 \times 1}$ in (29) are represented as

$$\mathbf{b}_p = [\mathbf{b}_{p,j}]^T \text{ with } \mathbf{b}_{p,j} = [w_{p,p}^j w_{v,p}^j r_{1,p}^j r_{2,p}^j]^T, \quad j = 1, \dots, 5 \quad (\text{D3a})$$

$$\mathbf{b}_i = [\mathbf{b}_{i,j}]^T \text{ with } \mathbf{b}_{i,j} = [w_{p,i}^j w_{v,i}^j r_{1,i}^j r_{2,i}^j]^T, \quad j = 1, \dots, 5 \quad (\text{D3b})$$

$$\mathbf{b}_d = [\mathbf{b}_{d,j}]^T \text{ with } \mathbf{b}_{d,j} = [w_{p,d}^j w_{v,d}^j r_{1,d}^j r_{2,d}^j]^T, \quad j = 1, \dots, 5. \quad (\text{D3c})$$

REFERENCES

- [1] H. W. Lee, K. C. Kim, and J. Lee, "Review of maglev train technologies," *IEEE Trans. Magn.*, vol. 42, no. 7, pp. 1917–1925, Jul. 2006.
- [2] I. Boldea and S. A. Nasar, "Linear electric actuators and generators," *IEEE Trans. Energy Convers.*, vol. 14, no. 3, pp. 712–717, Sep. 1999.
- [3] P. Holmer, "Faster than a speeding bullet train," *IEEE Spectr.*, vol. 40, no. 8, pp. 30–34, Aug. 2003.
- [4] F. J. Lin, R. J. Wai, W. D. Chou, and S. P. Hsu, "Adaptive backstepping control using recurrent neural network for linear induction motor drive," *IEEE Trans. Ind. Electron.*, vol. 49, no. 1, pp. 134–146, Feb. 2002.
- [5] R. J. Wai and W. K. Liu, "Nonlinear control for linear induction motor servo drive," *IEEE Trans. Ind. Electron.*, vol. 50, no. 5, pp. 920–935, Oct. 2003.
- [6] M. Y. Chen, M. J. Wang, and L. C. Fu, "Modeling and controller design of a maglev guiding system for application in precision positioning," *IEEE Trans. Ind. Electron.*, vol. 50, no. 3, pp. 493–506, Jun. 2003.
- [7] J. Kaloust, C. Ham, J. Siehling, E. Jongekryg, and Q. Han, "Nonlinear robust control design for levitation and propulsion of a maglev system," *Proc. Inst. Elect. Eng.—Control Theory Appl.*, vol. 151, no. 4, pp. 460–464, Jul. 2004.
- [8] M. Ono, S. Koga, and H. Ohtsuki, "Japan's superconducting maglev train," *IEEE Trans. Instrum. Meas. Mag.*, vol. 5, no. 1, pp. 9–15, Mar. 2002.
- [9] C. M. Huang, J. Y. Yen, and M. S. Chen, "Adaptive nonlinear control of repulsive maglev suspension systems," *Control Eng. Pract.*, vol. 8, no. 12, pp. 1357–1367, Dec. 2000.
- [10] H. Shakir and W. J. Kim, "Nanoscale path planning and motion control with maglev positioners," *IEEE/ASME Trans. Mechatronics*, vol. 11, no. 5, pp. 625–633, Oct. 2006.
- [11] X. Jie and B. T. Kulakowski, "Sliding mode control of active suspension for transit buses based on a novel air-spring model," in *Proc. IEEE Amer. Control Conf.*, 2003, vol. 5, pp. 3768–3773.
- [12] W. G. Hurley, M. Hynes, and W. H. Wolffe, "PWM control of a magnetic suspension system," *IEEE Trans. Educ.*, vol. 47, no. 2, pp. 165–173, May 2004.
- [13] D. L. Trumper, S. M. Olson, and P. K. Subrahmanyam, "Linearizing control of magnetic suspension systems," *IEEE Trans. Control Syst. Technol.*, vol. 5, no. 4, pp. 427–438, Jul. 1997.
- [14] M. S. Queiroz and D. M. Dawson, "Nonlinear control of active magnetic bearings: A backstepping approach," *IEEE Trans. Control Syst. Technol.*, vol. 4, no. 5, pp. 545–552, Sep. 1996.
- [15] J. Aracil, F. Gordillo, and E. Ponce, "Stabilization of oscillations through backstepping in high-dimensional systems," *IEEE Trans. Autom. Control*, vol. 50, no. 5, pp. 705–710, May 2005.
- [16] R. J. Wai and J. D. Lee, "Performance comparisons of model-free control strategies for hybrid magnetic levitation system," *Proc. Inst. Elect. Eng.—Elect. Power Appl.*, vol. 152, no. 6, pp. 1556–1564, Nov. 2005.
- [17] R. J. Wai and J. D. Lee, "Adaptive fuzzy-neural-network control for maglev transportation system," *IEEE Trans. Neural Netw.*, vol. 19, no. 1, pp. 54–70, Jan. 2008.
- [18] R. C. Eberhart and J. Kennedy, "A new optimizer using particles swarm theory," in *Proc. 6th Int. Symp. Micro Mach. Human Sci.*, 1995, pp. 39–43.
- [19] R. C. Eberhart and J. Kennedy, "Particle swarm optimization," in *Proc. IEEE Conf. Neural Netw.*, 1995, pp. 1942–1948.
- [20] Y. Shi and R. C. Eberhart, "A modified particle swarm optimizer," in *Proc. IEEE Conf. Comput. Intell.*, 1998, pp. 69–73.
- [21] A. E. Eiben, R. Hinterding, and Z. Michalewicz, "Parameter control in evolutionary algorithms," *IEEE Trans. Evol. Comput.*, vol. 3, no. 2, pp. 124–141, Jul. 1999.
- [22] Z. H. Zhan, J. Zhang, Y. Li, and H. Chung, "Adaptive particle swarm optimization," *IEEE Trans. Syst., Man, Cybern. B, Cybern.*, vol. 39, no. 6, pp. 1362–1381, Dec. 2009.
- [23] S. H. Ling, H. Iu, F. H. F. Leung, and K. Y. Chan, "Improved hybrid particle swarm optimized wavelet neural network for modeling the development of fluid dispensing for electronic packaging," *IEEE Trans. Ind. Electron.*, vol. 55, no. 9, pp. 3447–3460, Sep. 2008.
- [24] L. S. Coelho and B. M. Herrera, "Fuzzy identification based on a chaotic particle swarm optimization approach applied to a nonlinear yo-yo motion system," *IEEE Trans. Ind. Electron.*, vol. 54, no. 6, pp. 3234–3245, Dec. 2007.
- [25] H. M. Feng, "Self-generation RBFNs using evolutionary PSO learning," *Neurocomputing*, vol. 70, no. 1–3, pp. 241–251, Dec. 2006.
- [26] A. Chatterjee, K. Pulasighe, K. Watanabe, and K. Izumi, "A particle-swarm-optimized fuzzy-neural network for voice-controlled robot systems," *IEEE Trans. Ind. Electron.*, vol. 52, no. 6, pp. 1478–1489, Dec. 2005.
- [27] D. E. Goldberg, *Genetic Algorithms in Search, Optimization, and Machine Learning*. Reading, MA: Addison-Wesley, 1989.
- [28] Z. L. Gaing, "A particle swarm optimization approach for optimum design of PID controller in AVR system," *IEEE Trans. Energy Convers.*, vol. 19, no. 2, pp. 384–391, Jun. 2004.
- [29] F. J. Lin, L. T. Teng, J. W. Lin, and S. Y. Chen, "Recurrent functional-link-based fuzzy-neural-network-controlled induction-generator system using improved particle swarm optimization," *IEEE Trans. Ind. Electron.*, vol. 56, no. 5, pp. 1557–1577, May 2009.
- [30] Y. He and F. L. Luo, "Sliding-mode control for dc–dc converters with constant switching frequency," *Proc. Inst. Elect. Eng.—Control Theory Appl.*, vol. 153, no. 1, pp. 38–45, Jan. 2006.
- [31] G. Metin, B. Seta, and G. J. Douglas, "Sliding mode based power-train control for efficiency improvement in series hybrid-electric vehicles," *IEEE Trans. Power Electron.*, vol. 21, no. 3, pp. 779–790, May 2006.
- [32] K. J. Astrom and B. Wittenmark, *Adaptive Control*. New York: Addison-Wesley, 1995.
- [33] H. M. Gutierrez and P. I. Ro, "Magnetic servo levitation by sliding-mode control of nonaffine systems with algebraic input invertibility," *IEEE Trans. Ind. Electron.*, vol. 52, no. 5, pp. 1449–1455, Oct. 2005.
- [34] B. Bandyopadhyay, P. S. Gandhi, and S. Kurode, "Sliding mode observer based sliding mode controller for slosh-free motion through PID scheme," *IEEE Trans. Ind. Electron.*, vol. 56, no. 9, pp. 3432–3442, Sep. 2009.
- [35] J. Li, L. Xu, and Z. Zhang, "An adaptive sliding-mode observer for induction motor sensorless speed control," *IEEE Trans. Ind. Appl.*, vol. 41, no. 4, pp. 1039–1046, Jul./Aug. 2005.
- [36] R. J. Wai and L. J. Chang, "Adaptive stabilizing and tracking control for a nonlinear inverted-pendulum system via sliding-mode technique," *IEEE Trans. Ind. Electron.*, vol. 53, no. 2, pp. 674–692, Apr. 2006.
- [37] Y. X. Jin, H. Z. Cheng, J. Y. Yan, and L. Zhang, "Local optimum embranchment based convergence guarantee particle swarm optimization and its application in transmission network planning," in *Proc. IEEE PES Transmiss. Distrib. Conf. Exhib.*, 2005, pp. 1–6.
- [38] X. Chen and Y. Li, "A modified PSO structure resulting in high exploration ability with convergence guaranteed," *IEEE Trans. Syst., Man, Cybern. B, Cybern.*, vol. 37, no. 5, pp. 1271–1289, Oct. 2007.
- [39] F. P. Beer, E. R. Johnston, and W. E. Clausen, *Vector Mechanics for Engineers*. New York: McGraw-Hill, 2004.
- [40] J. Boeij, M. Steinbuch, and H. M. Gutierrez, "Mathematical model of the 5-DOF sled dynamics of an electrodynamic maglev system with a passive sled," *IEEE Trans. Magn.*, vol. 41, no. 1, pp. 460–465, Jan. 2005.

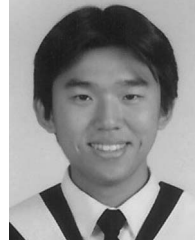


Rong-Jong Wai (M'99–SM'05) was born in Tainan, Taiwan, in 1974. He received the B.S. degree in electrical engineering and the Ph.D. degree in electronic engineering from Chung Yuan Christian University, Chung Li, Taiwan, in 1996 and 1999, respectively.

Since 1999, he has been with Yuan Ze University, Chung Li, where he is currently a Professor with the Department of Electrical Engineering, the Dean of the Office of General Affairs, the Chief of the Environmental Protection and Sanitation Office, and the Director of the Electric Control and System

Engineering Laboratory. He is a chapter-author of *Intelligent Adaptive Control: Industrial Applications in the Applied Computational Intelligence Set* (Boca Raton, FL: CRC Press, 1998) and the coauthor of *Drive and Intelligent Control of Ultrasonic Motor* (Tai-chung, Taiwan: Tsang-Hai, 1999), *Electric Control* (Tai-chung, Taiwan: Tsang-Hai, 2002), and *Fuel Cell: New Generation Energy* (Tai-chung, Taiwan: Tsang-Hai, 2004). He has authored numerous published journal papers in the area of control system applications. His biography was listed in *Who's Who in Science and Engineering* (Marquis Who's Who) in 2004–2009, *Who's Who* (Marquis Who's Who) in 2004–2009, *Leading Scientists of the World* (International Biographical Centre) in 2005, *Who's Who in Asia* (Marquis Who's Who), *Who's Who of Emerging Leaders* (Marquis Who's Who) in 2006–2009, and *Asia/Pacific Who's Who* (Rifacimento International) in Vols. VII and VIII. His research interests include power electronics, motor servo drives, mechatronics, energy technology, and control theory applications.

Dr. Wai received the Excellent Research Award in 2000 and the Wu Ta-You Medal and Young Researcher Award in 2003 from the National Science Council. In addition, he was the recipient of the Outstanding Research Award in 2003 and 2007 from Yuan Ze University; the Excellent Young Electrical Engineering Award in 2004 and the Outstanding Electrical Engineering Professor Award in 2010 from the Chinese Electrical Engineering Society; the Outstanding Professor Award in 2004 and 2008 from the Far Eastern Y. Z. Hsu-Science and Technology Memorial Foundation; the International Professional of the Year Award in 2005 from the International Biographical Centre, U.K.; the Young Automatic Control Engineering Award in 2005 from the Chinese Automatic Control Society; the Yuan-Ze Chair Professor Award in 2007 and 2010 from the Far Eastern Y. Z. Hsu-Science and Technology Memorial Foundation; the Electric Category-Invent Silver Metal Award in 2007; the Electronic Category-Invent Gold and Silver Metal Awards in 2008; the Environmental Protection Category-Invent Gold Metal Award in 2008; and the Most Environmental Friendly Award in 2008 from the International Invention Show and Technomart, Taipei; the University Industrial Economic Contribution Award in 2010 from the Ministry of Economic Affairs, Taiwan.



Jeng-Dao Lee (M'09) was born in Taipei, Taiwan, in 1980. He received the B.S. and Ph.D. degrees in electrical engineering from Yuan Ze University, Chung Li, Taiwan, in 2002 and 2007, respectively.

He is currently with the National Formosa University, Yunlin, Taiwan, where he is currently an Assistant Professor with the Department of Automation Engineering. His research interests include motor servo drives, power electronics, mechatronics, and intelligent control.



Kun-Lun Chuang was born in Hsin Chu, Taiwan, in 1983. He received the B.S. degree in electrical engineering from the Ming Hsin University of Science and Technology, Hsin Chu, in 2006 and the M.S. degree in electrical engineering from Yuan Ze University, Chung Li, Taiwan, in 2008.

He is currently with the Army, Ministry of National Defense, Taipei, Taiwan. His research interests include particle swarm optimization and maglev systems.